Title
Turbulent models of ice giant internal dynamics: Dynamos, heat transfer, and zonal flows

Journal
Icarus, 224(1)

ISSN
0019-1035

Authors
Soderlund, KM
Heimpel, MH
King, EM
et al.

Publication Date
2013-05-01

DOI
10.1016/j.icarus.2013.02.014

Peer reviewed

Icarus 224 (2013) 97–113

Contents lists available at SciVerse ScienceDirect

Icarus

journal homepage: www.elsevier.com/locate/icarus

Turbulent models of ice giant internal dynamics: Dynamos, heat transfer, and zonal flows

K.M. Soderlund [a,*], M.H. Heimpel [b], E.M. King [c], J.M. Aurnou [d]

[a] Institute for Geophysics, Jackson School of Geosciences, University of Texas at Austin, Austin, TX 78758, USA
[b] Department of Physics, University of Alberta, Edmonton, Alberta, Canada T6G 2J1
[c] Department of Earth and Planetary Science, University of California, Berkeley, CA 94720, USA
[d] Department of Earth and Space Sciences, University of California, Los Angeles, CA 90095, USA

ARTICLE INFO

Article history:
Received 10 October 2012
Revised 25 January 2013
Accepted 11 February 2013
Available online 27 February 2013

Keywords:
Atmospheres
Dynamics
Magnetic fields

ABSTRACT

The ice giant planets, Uranus and Neptune, have magnetic fields, atmospheric circulation patterns, and thermal emissions that are distinct from other planets in our Solar System. However, no self-consistent dynamical model has been able to reproduce all of these observations. We hypothesize that the dynamos and surface winds are dynamically coupled and argue that their characteristics are a consequence of three-dimensional turbulence that may be excited in planetary-scale water layers. Here we present dynamo models with thick and thin spherical shell geometries consistent with the range of possible internal structures of Uranus and Neptune. The style of convection is chosen a priori to yield small-scale and disorganized turbulence. In agreement with ice giant observations, both simulations (i) generate multipolar magnetic fields by fluctuating dynamo action, (ii) produce zonal jets with retrograde flow at the equator through angular momentum mixing, and (iii) predict local equatorial peaks in internal heat fluxes due to equatorial upwellings induced primarily by Hadley-like circulation cells. Thus, we argue that three-dimensional convective turbulence can explain the first-order geophysical observations of the ice giants.

1. Introduction

Planetary magnetic fields provide a means through which information about the interiors of planets can be remotely inferred. Three styles of magnetic field morphologies are observed in our Solar System. Earth, Ganymede, Jupiter, and Saturn have dipole-dominated magnetic fields that are nearly aligned with their rotation axes (e.g., Kivelson et al., 1996; Burton et al., 2009; Yu et al., 2010), while Mercury is dominated by axially aligned dipolar and quadrupolar field components (Anderson et al., 2011, 2012). Uranus and Neptune, the ice giants, are the only known planetary bodies in our Solar System to have strongly non-axisymmetric, multipolar magnetic fields (Ness et al., 1986, 1989; Holme and Bloxham, 1996). This study focuses on these latter dynamos.

1.1. Internal structures

The internal structures of the ice giants can be inferred from observations of their magnetic and gravity fields by Voyager 2. For example, the presence of an intrinsic magnetic field requires an electrically conducting fluid region. Gravity field measurements provide additional constraints and suggest that these planets may be modeled as three nested regions: (i) an outermost molecular envelope largely composed of hydrogen and helium; (ii) a weakly conducting ionic ocean of water, methane, and ammonia; and (iii) a rocky central core (e.g., Hubbard et al., 1991; Podolak et al., 1991; Guillot, 1999). Recent experiments suggest that the gradual transition between the molecular envelope and the underlying ionic ocean occurs near 0.8 planetary radii where the electrical conductivity reaches about 2500 S/m (e.g., Lee et al., 2006). The transition between the ionic ocean and rocky core is thought to occur below 0.3 planetary radii (e.g., Redmer et al., 2011). Sharp compositional transitions between these regions are not required (Helled et al., 2011), however, and the location of the triple point between ice, fluid, and superionic water is not well determined (Redmer et al., 2011). Schematics of possible internal structures of Uranus and Neptune are illustrated in Fig. 1 (top row).

Voyager 2 also measured the thermal energy emitted by the ice giants. While both planets emit nearly the same amount of total thermal energy (~5 PW; Pearl et al., 1990), their differing orbital radii imply a sharp contrast in their energy balance. Neptune emits more than twice the thermal energy it receives via insolation (Pearl

* Corresponding author. Fax: +1 512 471 8844.
E-mail addresses: krista@ig.utexas.edu (K.M. Soderlund), mheimpel@phys.ualberta.ca (M.H. Heimpel), eric.king@berkeley.edu (E.M. King), aurnou@ucla.edu (J.M. Aurnou).

0019-1035/$ - see front matter © 2013 Elsevier Inc. All rights reserved.
http://dx.doi.org/10.1016/j.icarus.2013.02.014

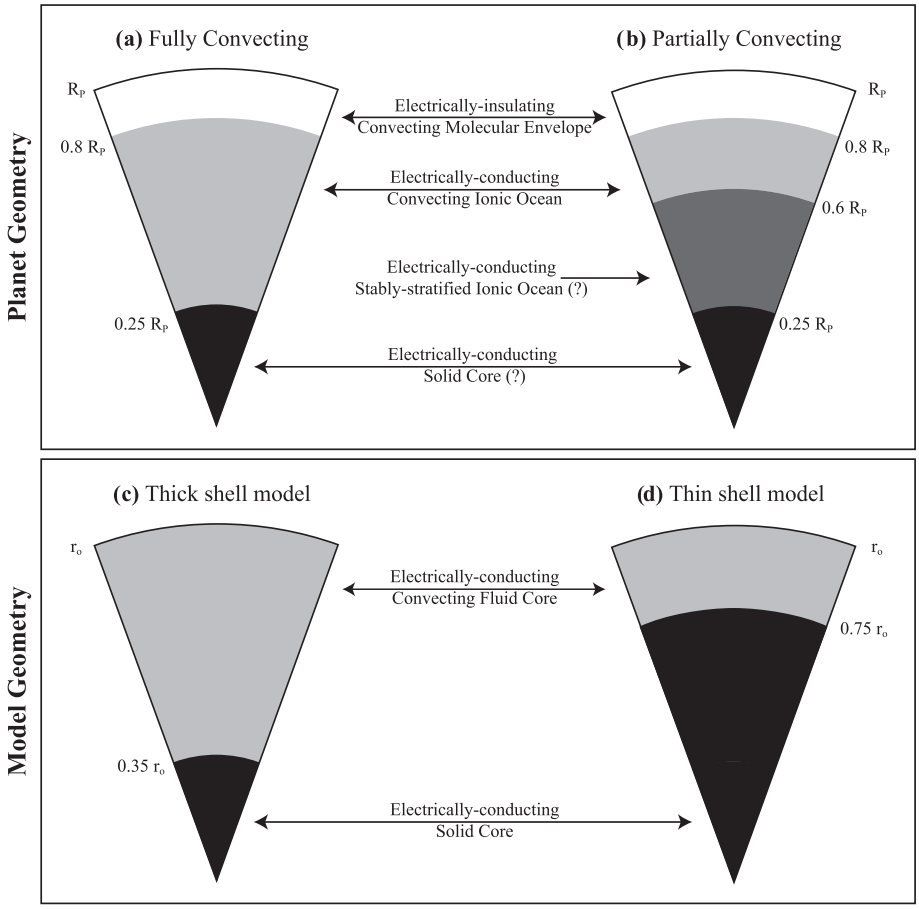

Fig. 1. Possible internal structure models of Neptune and Uranus based on Redmer et al. (2011); R_P is planetary radius. As discussed by Podolak et al. (1991) and Fortney et al. (2011) among others, the ionic oceans may be (a) fully convecting or (b) partially convecting. Geometry of the (c) thick shell and (d) thin shell numerical models. r_o is the outer shell radius of the model and is assumed to correspond to the planet surfaces, taken to be the 1 bar pressure level, in our simplified models that neglect electrical conductivity and density stratification.

and Conrath, 1991), while the total emission to insolation ratio for Uranus is no greater than ~1.1 (Pearl et al., 1990). Internal heat sources are implied for both planets, however, since these ratios exceed unity, likely due to the release of primordial heat of formation and radioactive heating. These measurements also indicate that the interiors of both Uranus and Neptune are unstable to convection since their internal (emitted minus absorbed) heat fluxes of 0.04 W/m^2 and 0.4 W/m^2, respectively, exceed the adiabatic heat flux estimates of $\simeq$0.01 W/m^2 (e.g., Stevenson, 1983). Differences in internal structures (regions of stable stratification; Stevenson, 1983; Podolak et al., 1991; Fortney et al., 2011; Nettelmann et al., 2012) or internal dynamics (baroclinic instabilities; Holme and Ingersoll, 1994) have been proposed to explain why Neptune emits significantly more heat than it receives from the Sun, while Uranus does not.

Since there are likely no sharp structural boundaries in the ice giants between the dynamo region and the overlying electrically insulating layer (cf. the core–mantle boundary of Earth), it is possible that the dynamo, heat flow, and atmospheric winds are all dynamically coupled together in these bodies. Further, if the magnetic fields are driven relatively near the surface, a single region may simultaneously generate these observables. In this unified layer scenario, surface winds may be driven by deep convection in the dynamo region through teleconvection (Zhang and Schubert, 2000, 2002; Stanley and Mohammadi, 2008; Takehiro et al., 2011), even if regions are stably stratified. Thus, we seek to generate single-layer models that can self-consistently explain all three of these geophysical observations. The magnetic fields, thermal emissions, and winds of the ice giants are described below.

1.2. Magnetic fields

The magnetic fields of Uranus and Neptune as measured by Voyager 2 in 1986 and 1989, respectively, are non-axisymmetric and multipolar with quadrupole and octupole components that are comparable to or greater than the dipole (Figs. 2 and 10). Spherical harmonics greater than the octupole are below the limits of spatial resolution, and there is no information about secular variation (Holme and Bloxham, 1996).

These magnetic fields are thought to result from convectively driven dynamo action in the ionic ocean (e.g., Ruzmaikin and Starchenko, 1991; Stanley and Bloxham, 2004; Jones, 2011). Shock experiments on precompressed water and ab initio simulations suggest that electrical conductivity is large enough to support dynamos in the ice giants at depths below about $0.8R_P$, where R_P ~ 25,000 km are the planetary radii (Cavazzoni et al., 1999; Lee et al., 2006; Redmer et al., 2011; Knudson et al., 2012). This relatively shallow dynamo region is consistent with the prominence of the higher order spherical harmonics of the planets' magnetic fields (Russell and Dougherty, 2010). The lower boundary of the dynamo generating region is more controversial, however, given the debate on whether the deep ionic ocean is convecting or stably stratified (e.g., Stanley and Bloxham, 2004; Redmer et al., 2011;

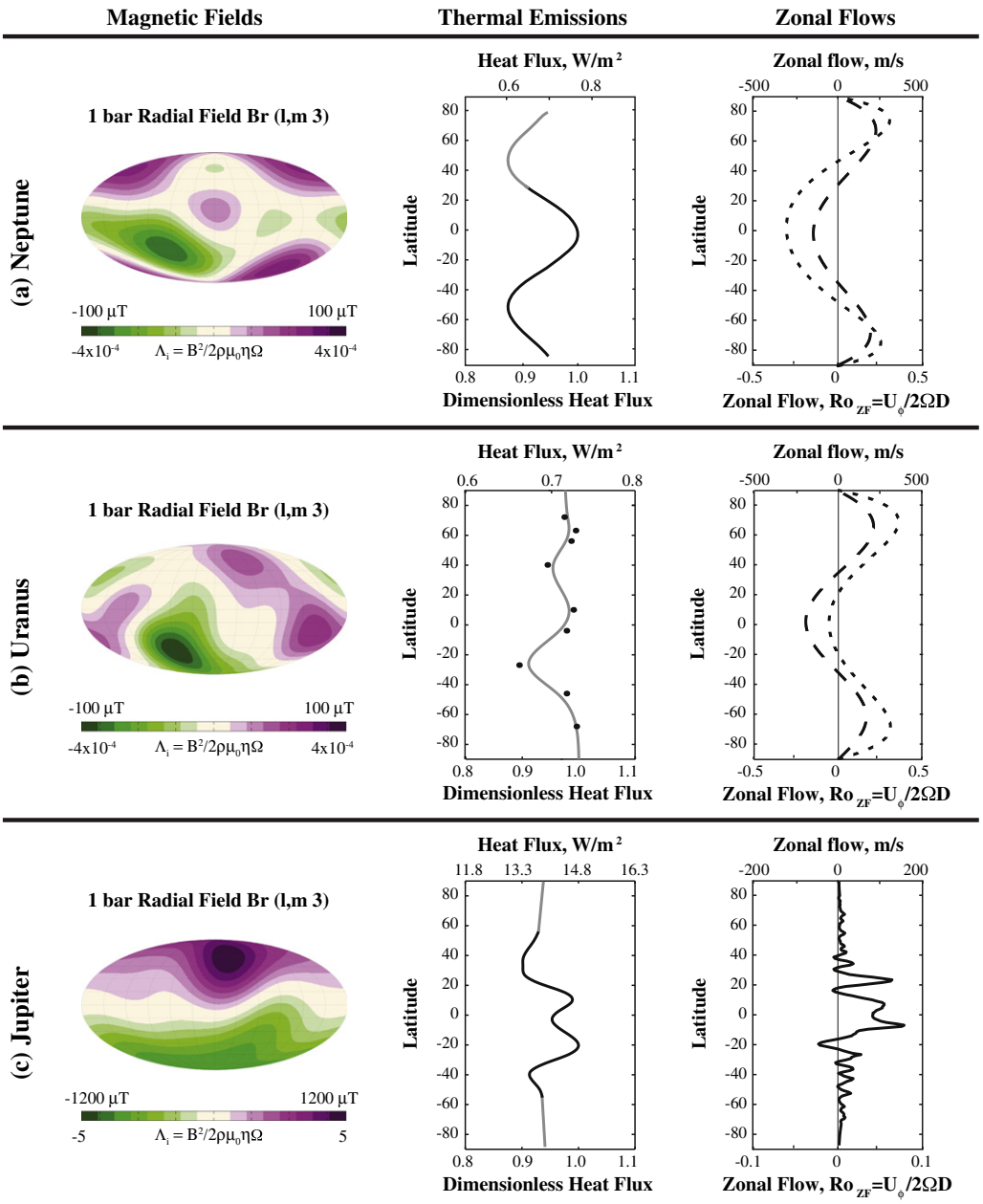

Fig. 2. Surface observations of radial magnetic fields, thermal emissions, and zonal winds of the ice giants and Jupiter. The dimensionless heat flux profiles have been normalized such that the maximum value is unity; extrapolated data shown in gray. Ro_{ZF} estimates assume that the winds extend to the bases of the molecular envelopes. Magnetic field data is from Holme and Bloxham (1996) and Yu et al. (2010); thermal emission data is from Pearl and Conrath (1991), Pearl et al. (1990) fit with a cubic spline, and Pirraglia (1984); and zonal wind data is from Sukoriansky et al. (2002) (short-dashed lines), Helled et al. (2010) (long-dashed lines), and Porco et al. (2003).

Chau et al., 2011; Fortney et al., 2011; Nettelmann et al., 2012). Thus, the dynamo region may have a thick or thin shell geometry.

1.3. Thermal emissions

The release of gravitational energy provides a source of internal heat in the giant planets (Stevenson, 1978), and convective motions redistribute this energy. As such, heat flux patterns provide insight into these convective processes. Fig. 2 also shows the thermal emissions measured by Voyager 2 as a function of latitude. Neptune preferentially emits heat from the equatorial and polar regions (Pearl and Conrath, 1991). This profile, however, assumes latitudinal symmetry across the equator since little data is available in the northern hemisphere. The heat flux pattern for Uranus is poorly constrained (Pearl et al., 1990).

1.4. Zonal winds

The surface zonal winds are determined by tracking cloud features over finite time intervals. Observations made by the Voyager 2 spacecraft, the Hubble Space Telescope, and ground-based telescopes have revealed that the surface winds are dominated by zonal (east–west) motions (e.g. Smith et al., 1986, 1989; Sromovsky et al., 2001, 2009; Hammel et al., 2001, 2005; Karkoschka, 2011; Fry et al., 2012; Martin et al., 2012). These zonal winds are measured with respect to the mean rotational motion of the planet, assumed to correspond with the deep-seated magnetic field frame of reference (e.g., Ness et al., 1994). Voyager 2 radio observations suggest that the rotation periods of Uranus and Neptune are, respectively, 17.24 h and 16.11 h (Desch et al., 1986; Warwick et al., 1989). Adopting these periods, both planets have retrograde (west-

ward) jets near the equator and prograde (eastward) jets at high latitudes, as shown in Fig. 2. Further, Neptune has the fastest wind speeds in the Solar System that approach −400 m/s in the equatorial jet and +250 m/s in the high latitude jets. Uranian winds have maximum velocities near +200 m/s in the high latitude jets and an equatorial jet speed of about −100 m/s.

There are complications, however, in determining the rotation rates from radio observations. For example, the radio emissions of Saturn have multiple periodicities and vary in time (Gurnett et al., 2007, 2009). Alternatively, dynamical arguments can be used to estimate the rotation periods (Helled et al., 2010; Karkoschka, 2011). Helled et al. (2010) estimate rotation periods by finding the rotation rate that produces the smallest deviation between the observed oblateness and that inferred from the body's rotation. This approach predicts periods that differ from those based on Voyager 2 radio signals by −40 min and +68 min for Uranus and Neptune, respectively. Further, Karkoschka (2011) estimates the rotation period of Neptune to be 15.97 h, a difference of −8 min from the Voyager 2 derived period, by tracking features (e.g., storms) and noting their rotational stabilities. These differences illustrate the uncertainties in giant planet rotation rates, which are reflected in the zonal winds. Adopting the Helled et al. (2010) rotation periods, both Uranus and Neptune have retrograde equatorial jets with speeds of about −150 m/s and prograde high latitude jets with peak speeds of about +200 m/s. Zonal wind profiles assuming the Helled et al. (2010) rotation periods are superimposed in Fig. 2 to illustrate these differences.

The winds measured near the surface may be linked to convection in their interiors. Karkoschka (2011) argues that the stationary features found in Hubble Space Telescope images of Neptune may result from deep convective processes. Furthermore, the dominant motions observed on both Uranus and Neptune are perpendicular to the rotation axis, despite Uranus' dramatically different pattern of solar heating due to the planet's 98° inclination with respect to the ecliptic. Instead of time-averaged insolation peaking near the equator as for the other planets, Uranus' polar and equatorial regions receive comparable amounts of sunlight over a uranian year (e.g., Levine et al., 1977). This suggests that the winds may have a deep origin.

1.5. Comparison against the gas giants

The observations of Uranus and Neptune are fundamentally different from those of the gas giants, demonstrated in Fig. 2 by the inclusion of jovian observations. In contrast to the multipolar dynamos of the ice giants, Jupiter's magnetic field is dipole-dominated with the dipole tilted about 10° from the rotation axis. Similarly, Jupiter's surface winds are organized into a strong prograde equatorial jet and multiple jets at high latitudes that alternate in direction (Porco et al., 2003). Efforts toward understanding the dynamics of the ice giants must then also explain why these bodies are different from those of the gas giants.

We argue that the differences in surface magnetic fields, heat transfer, and zonal winds between the ice and gas giants can be explained by a difference in interior dynamics in Section 2. The numerical model used to test this hypothesis is detailed in Section 3. Section 4 describes the simulated magnetic, temperature, and velocity field characteristics, while Section 5 investigates their generation. Section 6 compares our results against observations, and conclusions are given in Section 7.

2. Regimes of convective dynamics

Here we test the hypothesis of Aurnou et al. (2007) that the internal dynamics of the ice giants are influenced to a lesser degree by planetary rotation in comparison to the gas giants. Arguments in favor of this hypothesis are derived from a number of sources, including observations of the surface winds, scaling laws for the

Table 1
Summary of non-dimensional parameters. Input (output) parameters are given above (below) the dashed line.

Definition	Interpretation	Model
$\chi = r_i/r_o$	Shell geometry	[0.35, 0.75]
$E = \nu/2\Omega D^2$	Viscous/Coriolis forces	1.5×10^{-4}
$Pr = \nu/\kappa$	Viscous/thermal diffusivities	1
$Pm = \nu/\eta$	Viscous/magnetic diffusivities	[0,1]
$Ra = \alpha g_o \Delta T D^3/\nu\kappa$	Buoyancy/diffusion	2.22×10^7
$Ro_c = \sqrt{\frac{\alpha g \Delta T}{4\Omega^2 D}} = \sqrt{RaE^2/Pr}$	Buoyancy/Coriolis forces	0.71
$\Psi_{King} \approx 0.3 Ro_c E^{-1/4} Pr^{1/2}$	Transition parameter (King et al., 2012)	1.9
$\Psi_{Julien} \approx Ro_c E^{-1/5} Pr^{1/2}$	Transition parameter (Julien et al., 2012a)	4.1
$\Psi_{ST}^{Nu} \approx 0.7 RoE^{-1/2} Pr$	Transition parameter (Schmitz and Tilgner, 2010)	
$\Psi_{ST}^{H} \approx 0.03 RoE^{-1/2}$	Transition parameter (Schmitz and Tilgner, 2010)	
$\mathscr{E}_K = \frac{1}{2V}\int \mathbf{u}\cdot\mathbf{u}\, dV$	Kinetic energy density	
$\mathscr{E}_M = \frac{1}{2V}\int \mathbf{B}\cdot\mathbf{B}\, dV$	Magnetic energy density	
$\overline{k_u} = \sqrt{\frac{\sum \overline{l(\mathbf{u}_l\cdot\mathbf{u}_l)2}}{2\mathscr{E}_K} + \frac{\sum \overline{m(\mathbf{u}_m\cdot\mathbf{u}_m)2}}{2\mathscr{E}_K}}$	Characteristic kinetic wavenumber	
$\overline{k_B} = \sqrt{\frac{\sum \overline{l(\mathbf{B}_l\cdot\mathbf{B}_l)2}}{2\mathscr{E}_M} + \frac{\sum \overline{m(\mathbf{B}_m\cdot\mathbf{B}_m)2}}{2\mathscr{E}_M}}$	Characteristic magnetic wavenumber	
$\ell_B = (\pi D/2)/\overline{k_B}$	Length scale of magnetic field variations	
$Nu = \frac{r_i}{r_o} QD/\rho C_p \kappa \Delta T$	Total/conductive heat transfer	
$Re = UD/\nu = \sqrt{2\mathscr{E}_K}$	Inertial/viscous forces	
$Rm = UD/\eta = RePm$	Magnetic induction/magnetic diffusion	
$Ro = U/2\Omega D = ReE$	Inertial/Coriolis forces	
$Ro_{ZF} = U_\phi/2\Omega D$	Zonal inertial/Coriolis forces	
$\Lambda_i = B^2/2\rho\mu_o\eta\Omega = \mathscr{E}_M PmE$	Lorentz/Coriolis forces (low Rm limit)	
$\Lambda_d = B^2/2\rho\mu_o\Omega U\ell_B = \frac{\Lambda_i}{Rm}\frac{D}{\ell_B}$	Lorentz/Coriolis forces (high Rm limit)	
$F^\phi = \int_0^\pi \int_{r_i}^{r_o} \lvert\mathscr{F}(r,\theta)\rvert r^2 \sin\theta dr d\theta$	Zonal force amplitude	
$Q_d = F_L^\phi/F_V^\phi$	Zonal Lorentz/zonal viscous forces	

behavioral style of rotating convection, and planetary dynamo simulations.

First, let us consider the zonal wind speeds as measured by the zonal Rossby number. This parameter characterizes the ratio of inertial to Coriolis forces: $Ro_{ZF} = U/2\Omega D$, where U and D are characteristic zonal velocities and fluid layer depths, respectively. Assuming that the observed winds extend at least to the bases of the molecular envelopes (cf. Lian and Showman, 2010; Gastine et al., 2012), the strong ice giant zonal winds have $|Ro_{ZF}| \gtrsim 0.1$ on average, while the slower jovian zonal winds have $|Ro_{ZF}| \ll 1$ (Fig. 2). These estimates imply that rotation has a weaker role in the ice giants than the gas giants or, conversely, that inertia has a more substantial role.

Rotating convection scaling laws, which are a subject of current debate and based upon studies in plane layer or right cylindrical geometries, also suggest that different styles of convection (e.g., quasi-two-dimensional versus three-dimensional flow structures) can exist in the interiors of gas and ice giant planets. The convective regime transition is traditionally thought to be determined by the ratio of buoyancy to Coriolis forces, characterized by the convective Rossby number

$$Ro_c = \left(\frac{\alpha g_o \Delta T}{4\Omega^2 D}\right)^{1/2} = \sqrt{\frac{RaE^2}{Pr}}, \tag{1}$$

with the transition at $Ro_c \sim 1$ (e.g., Gilman, 1977, 1978; Aurnou et al., 2007; Zhong and Ahlers, 2010; Weiss et al., 2010). Here, α is thermal expansion coefficient, g_o is gravitational acceleration, ΔT is superadiabatic temperature contrast, Ω is rotation rate, and D is characteristic length scale. This expression can also be recast in terms of other dimensionless parameters (see Table 1): the Rayleigh number, Ra, characterizes the ratio of buoyancy to diffusion; the Ekman number, E, characterizes the ratio of viscous to Coriolis forces; and the Prandtl number, Pr, characterizes the ratio of viscous to thermal diffusivities. Recent studies, however, have shown that the convective Rossby number fails to accurately predict the parameter values where the velocity and heat transfer behaviors characteristically change (e.g., Sprague et al., 2006; King et al., 2009, 2012; Schmitz and Tilgner, 2009, 2010; Julien et al., 2012a,b).

King et al. (2009, 2012) instead argue that the convective regime transition is controlled by boundary layer dynamics using theory and convection experiments. Three-dimensional turbulence is predicted to occur when the thermal boundary layer becomes convectively unstable at a transitional Rayleigh number of $Ra_T \approx 10E^{-3/2}$ (King et al., 2012). Using (1), this leads to a criterion of

$$\Psi_{King} = Ro_c/Ro_{c,T} \approx 0.3 Ro_c E^{-1/4} Pr^{1/2} \gtrsim 1. \tag{2}$$

Note that, for moderate Prandtl numbers, this criterion is easier to satisfy than $Ro_c > 1$, such that three-dimensional turbulence is more accessible than predicted by traditional arguments.

Asymptotic analyses of Rayleigh–Bénard convection also support the importance of boundary layer dynamics for the transition to three-dimensional turbulence. Julien et al. (2012a,b) argue that the transition occurs when the local convective Rossby number in the thermal boundary layer, *not* in the bulk fluid, exceeds unity. This criterion can be expressed as

$$\Psi_{Julien} \approx Ro_c E^{-1/5} Pr^{1/2} \gtrsim 1 \tag{3}$$

and corresponds to the loss of rotational constraint on the thermal boundary layer, similar to the scaling derived independently by King et al. (2012).

In contrast, Schmitz and Tilgner (2009, 2010) derive empirical scaling laws from numerical simulations of Rayleigh–Bénard convection with both no-slip and stress-free boundary conditions to predict the convective regime transition. These scalings suggest that the transition in heat transfer behavior as measured by the Nusselt number follows:

$$\Psi_{ST}^{Nu} \approx 0.7 RoE^{-1/2} Pr \gtrsim 1, \tag{4}$$

while the transition in flow structures as measured by helicity follows:

$$\Psi_{ST}^{H} \approx 0.03 RoE^{-1/2} \gtrsim 1. \tag{5}$$

Table 2
Order of magnitude estimates of the Rossby numbers for the planets' dynamo regions and the transition parameters of King et al. (2012), Julien et al. (2012a), and Schmitz and Tilgner (2010) defined in (1)–(5). The $Ro_c \sim Ro$ estimates are obtained by assuming $Rm = RePm = RoPm/E = 10^3$ with $E = [10^{-19}, 10^{-18}, 10^{-16}, 10^{-16}]$, $Pm = [10^{-7}, 10^{-7}, 10^{-8}, 10^{-8}]$, and $Pr = [0.1, 0.1, 10, 10]$ for [Jupiter, Saturn, Uranus, Neptune] taken from Schubert and Soderlund (2011). Our $Pm = 1$ dynamo simulations also have $Rm \sim 10^3$; this similarity between simulated and planetary magnetic Reynolds numbers is the foundation of the common assumption that no fundamental changes occur as model results are extrapolated toward planetary parameters (e.g., Christensen and Wicht, 2007; Calkins et al., 2012).

Dynamo region	Ro_c	Ψ_{King}	Ψ_{Julien}	Ψ_{ST}^{Nu}	Ψ_{ST}^{H}
Jupiter	10^{-9}	10^{-5}	10^{-6}	10^{-1}	10^{-1}
Saturn	10^{-8}	10^{-5}	10^{-5}	10^{0}	10^{-1}
Uranus	10^{-5}	10^{-1}	10^{-1}	10^{4}	10^{1}
Neptune	10^{-5}	10^{-1}	10^{-1}	10^{4}	10^{1}
Models	0.7	2	4	~10	~1

These criteria are applied to the giant planets in Table 2. Rough estimates of the convective Rossby number in the deep dynamo-generating regions of the giant planets suggest $Ro_c^{gas} \ll Ro_c^{ice} \ll 1$, implying rotationally constrained dynamics with rotation playing a stronger role at Jupiter and Saturn. In contrast, the ice giants are near the $\Psi \gtrsim 1$ criteria while the gas giants tend to be below, implying that rotation plays a weaker role at Uranus and Neptune as hypothesized.

Numerical simulations also suggest that the giant planet dichotomy may result from differences in their convective behaviors. Models of rotationally dominated convection with columnar flow structures are able to generate large-scale magnetic fields (Stanley and Glatzmaier, 2010; Heimpel and Gomez-Perez, 2011), internal heat flux patterns (Aurnou et al., 2008), and zonal flows (Heimpel et al., 2005b; Jones and Kuzanyan, 2009; Stanley and Glatzmaier, 2010) that are similar to those of Jupiter and Saturn. The success of these models to explain the observations of the gas giants raises the following question: Does a distinct dynamical regime exist which can explain the ice giant observations?

A dramatically different style of convection occurs when the columnar style of convection breaks down (e.g., Sprague et al., 2006; Soderlund et al., 2012; King and Aurnou, 2012; Julien et al., 2012b), typically achieved by increasing the thermal forcing. Strongly driven convective turbulence in rotating spherical shells can drive ice giant-style zonal flows (Aurnou et al., 2007; Brun and Palacios, 2009; Kaspi et al., 2009; Käpylä et al., 2011; Bessolaz and Brun, 2011; Gastine et al., 2012). Furthermore, dynamo models tend to produce multipolar magnetic fields when inertia is important (e.g., Grote et al., 1999, 2000; Christensen et al., 1999; Kutzner and Christensen, 2000, 2002; Stanley and Bloxham, 2004, 2006; Simitev and Busse, 2005; Christensen and Aubert, 2006; Olson and Christensen, 2006; Sreenivasan and Jones, 2006; Gomez-Perez and Heimpel, 2007; Soderlund et al., 2012; Dharmaraj and Stanley, 2012, cf. Guervilly et al., 2011). Thus, here we test the hypothesis that convection in planetary dynamo models characterized by three-dimensional turbulence will generate magnetic field morphologies, heat flux patterns, and zonal flows that are consistent with observations of the ice giants.

3. Numerical model

3.1. Governing equations

The dimensionless governing equations for thermal convection and dynamo action of a Boussinesq fluid in a spherical shell rotating at a fixed rate Ω about the axial $\hat{\mathbf{z}}$ direction are:

$$E\left(\frac{\partial \mathbf{u}}{\partial t}+\mathbf{u}\cdot\nabla\mathbf{u}-\nabla^2\mathbf{u}\right)+\hat{\mathbf{z}}\times\mathbf{u}+\frac{1}{2}\nabla\Pi = \frac{RaE}{Pr}\frac{\mathbf{r}}{r_o}T+\frac{1}{2Pm}(\nabla\times\mathbf{B})\times\mathbf{B}, \tag{6}$$

$$\frac{\partial T}{\partial t}+\mathbf{u}\cdot\nabla T=\frac{1}{Pr}\nabla^2 T, \tag{7}$$

$$\frac{\partial \mathbf{B}}{\partial t}=\nabla\times(\mathbf{u}\times\mathbf{B})+\frac{1}{Pm}\nabla^2\mathbf{B}, \tag{8}$$

$$\nabla\cdot\mathbf{u}=0,\quad \nabla\cdot\mathbf{B}=0, \tag{9}$$

where $\mathbf{u}$ is the velocity vector, $\mathbf{B}$ is the magnetic induction, T is the temperature, and Π is the non-hydrostatic pressure (e.g., Olson et al., 1999). Gravity is assumed to increase linearly with spherical radius and has a value of g_o on the outer boundary. The equations have been non-dimensionalized by shell thickness $D = r_o - r_i$ as length scale, ΔT as temperature scale, $\tau_\nu \sim D^2/\nu$ as time scale, ν/D as velocity scale, $\rho\nu\Omega$ as pressure scale, and $\sqrt{2\rho\mu_o\eta\Omega}$ as magnetic induction scale. Dimensionless rms velocity is then measured by the Reynolds number, $Re = UD/\nu$, and dimensionless rms magnetic field strength is measured by the square root of the traditional Elsasser number, $\Lambda_i = B^2/2\rho\mu_o\eta\Omega$. The four dimensionless control parameters, defined in Table 1, are:

$$Ra=\frac{\alpha g_o \Delta T D^3}{\nu\kappa},\quad E=\frac{\nu}{2\Omega D^2},\quad Pr=\frac{\nu}{\kappa},\quad Pm=\frac{\nu}{\eta}. \tag{10}$$

In these definitions, r_o is the outer shell radius, r_i is the inner shell radius, ν is kinematic viscosity, κ is thermal diffusivity, η is magnetic diffusivity, and α is thermal expansion coefficient.

Shell geometry is defined by the radius ratio of inner to outer shells, $\chi = r_i/r_o$. Two geometries are considered, shown in Fig. 1 (bottom row), in order to investigate the influence of convective-region geometry: a thick shell with $\chi = 0.35$ and a thin shell with $\chi = 0.75$. Boundary conditions are free-slip and isothermal. The solid, co-rotating inner sphere has the same electrical conductivity as the fluid outer shell.

The Boussinesq approximation is employed, where radial variations in electrical conductivity and density are neglected. This assumption is not physically realistic for ice giants, however, since the electrical conductivity varies by several orders of magnitude between the surface and the dynamo region (e.g., Cavazzoni et al., 1999). In addition, roughly one density scale height is expected in the ice giants' dynamo regions (Hubbard et al., 1991; Helled et al., 2011), while their molecular envelopes may extend across $\gtrsim 5$ scale heights (Helled et al., 2011). However, Jones and Kuzanyan (2009) and Gastine et al. (2012) show that anelastic and Boussinesq models of convection in giant planets yield similar results. Thus, we consider it important to first test our hypothesis without the additional complications that arise due to rapid variations in fluid properties.

In order to better understand the effects of magnetic fields on convective and zonal flow dynamics, we consider both dynamo and non-magnetic convection models by fixing the magnetic Prandtl number to $Pm = [1, 0]$. If the dynamics are found to be similar between the dynamo and non-magnetic models, electrical conductivity stratification will have only second-order effects on the hydrodynamics. In that case, our simplified dynamo models may be able to explain the basic global surface observations (magnetic field, thermal emission, and zonal flow patterns) of the ice giants.

In all of our models, the control parameters are fixed to $Ra = 2.22 \times 10^7$, $E = 1.5 \times 10^{-4}$, and $Pr = 1$. This choice of parameters selects three-dimensional turbulences since the transition parameters are all near unity (see Table 2). The models are strongly supercritical with $Ra = 110Ra_c$ for the thick shell cases and $Ra = 190Ra_c$ for the thin shell cases. The critical Rayleigh numbers, Ra_c, which denote the onset of convection, were estimated using the results of Al-Shamali et al. (2004) for non-magnetic rotating convection models with our E, Pr, and χ parameters.

3.2. Numerical method

Eqs. (6)–(9) are solved simultaneously for $\mathbf{u}$, $\mathbf{B}$, and T using the pseudospectral numerical model MagIC version 3.44 (e.g., Wicht, 2002; Christensen and Wicht, 2007). The velocity and magnetic field vectors are represented by toroidal and poloidal scalars. These four scalars and the temperature field are expanded in spherical harmonics with maximum degree and order l_{max} in the lateral directions and in Chebyshev polynomials in the radial direction up to degree $N_r - 2$, where N_r is the number of radial grid points across the fluid shell.

MagIC utilizes mixed implicit and explicit time stepping. The Coriolis and nonlinear terms are treated explicitly using a second-order Adams–Bashforth scheme and the diffusion, pressure, and linear terms are treated implicitly using a Crank–Nicolson time step. The implicit time step can vary over time and is limited by a modified MHD Courant criterion which accounts for viscous and ohmic damping of short-wavelength Alfvén-type oscillations (Christensen et al., 1999). This damping allows the use of a slightly larger numerical time step compared to the unmodified MHD Courant criterion. The code also utilizes OpenMP parallelization.

The thick shell simulations use a numerical grid with 192 spherical harmonic modes, 65 radial levels in the fluid outer shell, and 17 radial levels in the solid inner core; the resolution is increased to 213 harmonic modes for the thin shell simulations. No azimuthal symmetries or hyperdiffusivities are employed. The simulations are thought to have adequate spatial resolution since there is at least an order of magnitude difference between the maximum and the cut-off power (Christensen et al., 1999). Dynamo simulations are initialized using the results of prior dynamo models with three-dimensional convection and multipolar magnetic fields. The seed magnetic field morphology does not appear to impact the model results since a test case with an initial axial dipole field also produced a multipolar dynamo. Non-magnetic simulations are initialized by changing the electrical conductivity of a given dynamo model ($Pm = 1$) to be insulating ($Pm = 0$) and letting the system re-equilibrate.

Mean quantities are averaged in time once the initial transient behavior has subsided. The averaging windows are $[1.4, 0.4, 0.8, 0.5]$ viscous diffusion times, τ_ν, for the thick dynamo, thick non-magnetic, thin dynamo, and thin non-magnetic models, respectively, unless otherwise stated. These windows correspond to $[0.6, 0.05]$ magnetic diffusion times, τ_η, for the thick and thin shell dynamo models, respectively, where $\tau_\eta = \tau_\nu Pm/(1-\chi)^2$ following Heimpel et al. (2005a). While this thin shell window is short, the absence of long-term dipoles facilitates the averaging.

3.3. Dimensional analysis

To promote comparison between our simulations and planetary observations, numerical outputs are often *re-dimensionalized* (e.g., Jones and Kuzanyan, 2009; Jones et al., 2011). This process is limited by two obstacles. First, there is no unique way to deconvolve the absolute magnitudes of the dimensional physical constants

from which each dimensionless group is constructed. Second, the dimensionless parameters for convection on Uranus and Neptune are more extreme than can be accomplished computationally. If the simulations were dynamically similar to planetary systems, re-dimensionalizing the simulated system would return quantities that would all be similar to planetary values. However, since a number of the dimensionless parameters actually differ significantly from planetary values, re-dimensionalization may return some – but not all – dimensional quantities that are similar to planetary values. The non-unique choices made in re-dimensionalizing the system allow us to select which quantities we will likely get "right", and which we get wrong.

The choice that is almost ubiquitously made is to assume that the diffusive properties of the fluid are far higher than their molecular values. This is done because it is argued that diffusive processes are controlled by turbulent macro-scale transport in planetary settings (e.g., Roberts and Aurnou, 2012), although there exists little experimental evidence to support such arguments. Assuming that the loss of dynamic similarity between models and planets is due entirely to diffusivity differences, $E = 1.5 \times 10^{-4}$ requires an effective viscous diffusivity $\nu = [8 \times 10^6, 10^6]$ m^2/s and layer thickness $D = [1.6 \times 10^7, 6.3 \times 10^6]$ m in the $\chi = [0.35, 0.75]$ models, respectively, if we use ice giant values for the angular velocity $\Omega \simeq 10^{-4}$ s^{-1}. Since we set $Pr = Pm = 1$, the magnetic and thermal diffusivities are $\eta = \kappa = [8 \times 10^6, 10^6]$ m^2/s as well. These diffusivities are roughly 10^4–10^{13} times their molecular values, all far higher than physically-based estimates of turbulent diffusivities (e.g., Buffett and Christensen, 2007; Roberts and Aurnou, 2012).

The re-dimensionalization scheme above is used throughout this paper. The velocity scale is $\nu/D \sim [0.5, 0.2]$ m/s, and the magnetic induction scale is $\sqrt{2\rho\mu_o\eta\Omega} \sim [1.4, 0.5]$ T. Typical dimensionless flow speeds in our models are $Re \sim 10^3$, corresponding to [500,200] m/s. Since the dimensional velocities in our models are comparable to planetary values (Fig. 2), we argue that the models are *kinematically* realistic. Typical magnetic field strengths are $\Lambda_i \sim [2, 7]$, corresponding to roughly 1 T in both models. This overestimation occurs because η is more than ten thousand times larger in our models than in the ice giants. The heat fluxes required to achieve realistic flow speeds in these strongly diffusive fluids are also extremely large. The estimated superadiabatic heat flux in our models, q, can be estimated using the Nusselt number (Nu, see Table 1) to be of the order

$$q \simeq \frac{Nu}{\chi}\frac{\kappa\Delta T}{D} \simeq \frac{NuRa}{\chi}\frac{\rho C_p \nu\kappa^2}{\alpha g_o D^4} \sim \frac{NuRaE^3}{\chi Pr^2}\left(\frac{\rho C_p \Omega^3 D^2}{\alpha g_o}\right), \tag{11}$$

yielding $\sim 10^8$ W/m^2 in the thick shell models and $\sim 10^7$ W/m^2 in the thin shell models assuming density $\rho \sim 10^3$ kg/m^3, specific heat capacity $C_p \sim 10^3$ W/kg K, thermal expansivity $\alpha \sim 10^{-3}$ K^{-1}, and gravitational acceleration $g_o \sim 10$ m/s^2. Clearly, the superadiabatic heat fluxes required to drive kinematically realistic, ice giant-like flows in this highly viscous numerical fluid are far larger than the heat flux estimates of 0.4 and 0.04 W/m^2 for Neptune and Uranus, respectively.

However, the large heat fluxes required in our models do not imply that unrealistic heat fluxes are required to drive three-dimensional convection in the ice giant interiors (e.g., see Section 2 and Table 2). A different question can then be asked: Are such flows similar at planetary conditions (i.e., $E \simeq 10^{-16}$) and at presently accessible numerical conditions ($E \simeq 10^{-4}$)? Here, we make the assumption that the largest-scale flows in our models are kinematically similar to ice giant flows at first-order, as befits the relatively low resolution ice giant observations.

4. Model results

The characteristics of our models' magnetic, temperature, and velocity fields are described in this section. Table 3

Table 3
Dynamical characteristics of our models. Note that $Rm = Re$ in the dynamo cases since $Pm = 1$. Non-magnetic ($Pm = 0$) values are given in parentheses. The parameters are defined in Table 1, and all quantities are time-averaged.

χ	Re	Ro_{ZF}	Nu	$\overline{k_u}$	$\overline{k_B}$	Λ_i	Λ_d	Q_ϕ
0.35	955	−0.25	13.4	5.5	26	1.9	0.03	0.85
	(1094)	(−0.28)	(13.1)	(5.4)				
0.75	1133	−0.41	24.8	27	93	7.3	0.38	3.4
	(3134)	(−0.74)	(27.4)	(26)				

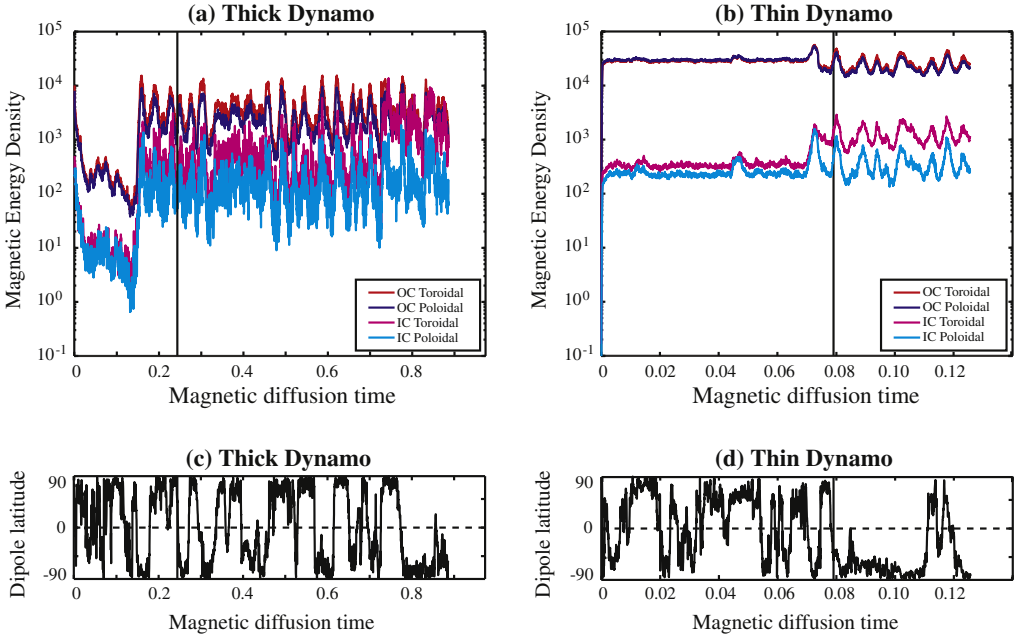

Fig. 3. Top row: time series of dimensionless magnetic energy density for the (a) thick and (b) thin shell dynamo models. Toroidal and poloidal components are shown for the outer (OC) and inner (IC) cores. Black vertical lines indicate where time-averaging begins. The transient is evident in (a) as the system equilibrates from its initial state; the change in behavior in (b) coincides with an increase in spatial resolution. Bottom row: time series of dipole latitude for the (c) thick and (d) thin shell dynamo models.

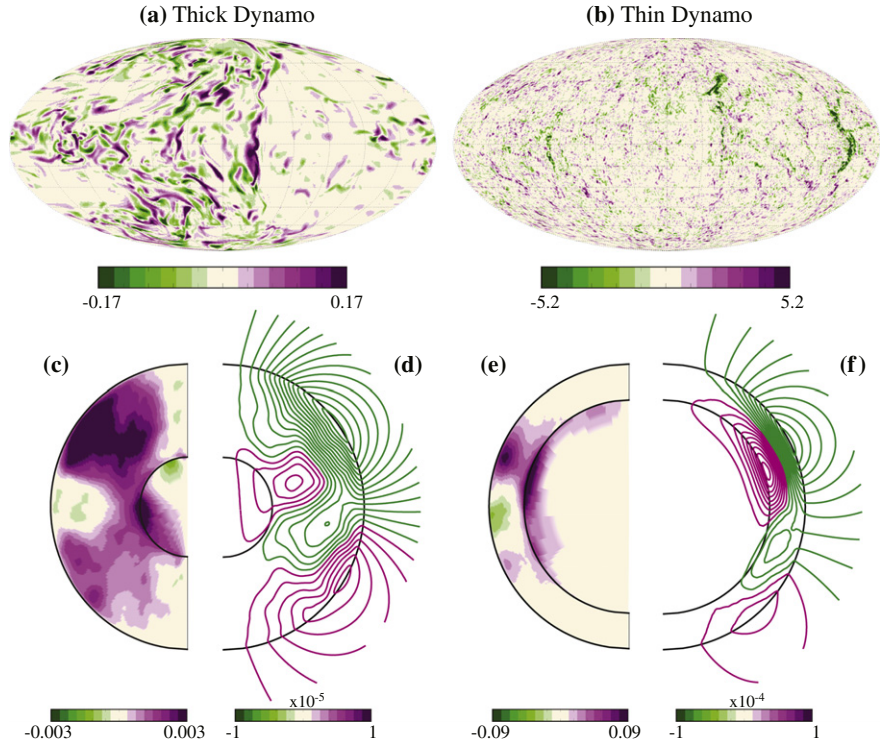

Fig. 4. Snapshots of the radial magnetic fields at the fifth radial levels below the outer surfaces, $r = 0.998r_o$, in the (a) thick and (b) thin shell dynamo models. Axisymmetric toroidal magnetic fields (c and e) and axisymmetric poloidal magnetic field lines (d and f) averaged over roughly 0.02 (0.004) magnetic diffusion times in the thick (thin) shell dynamo models. Magnetic field strengths are measured in dynamic Elsasser number units, Λ_d.

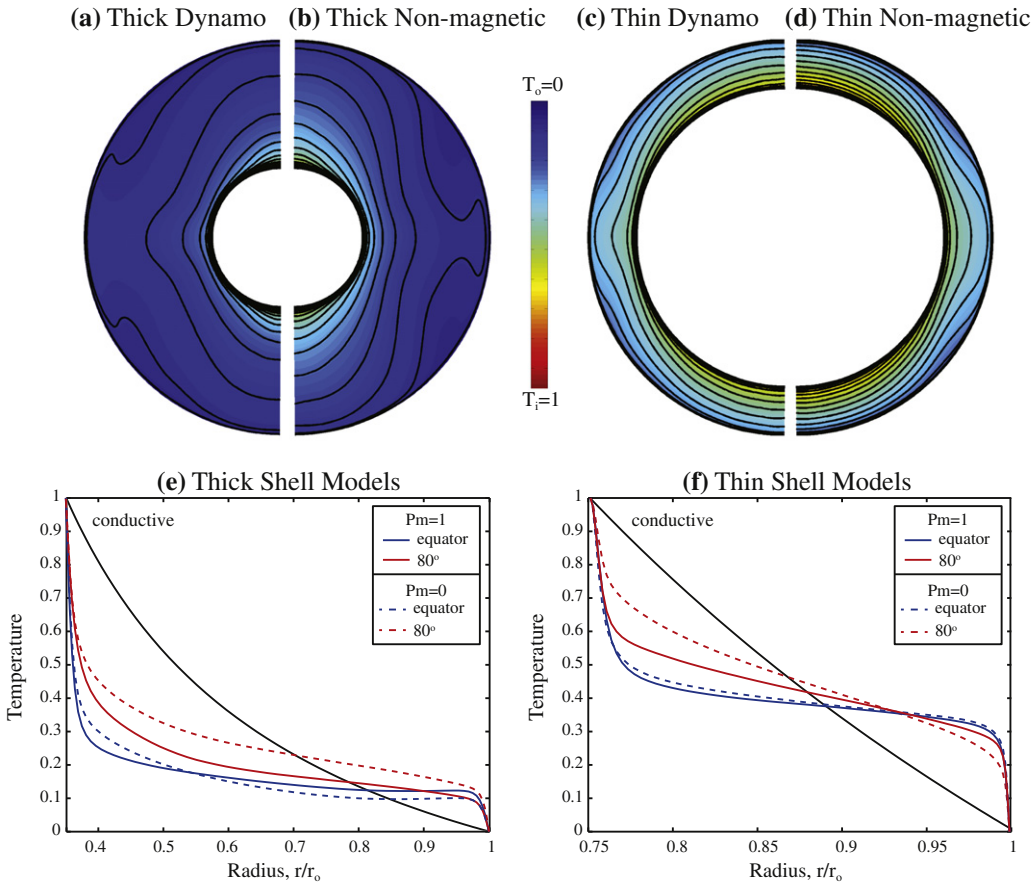

Fig. 5. (a–d) Time-averaged, axisymmetric mean temperatures, $(T - T_o)/\Delta T$, in the meridional planes of our models. Mean temperature as a function of radius at the equator and the average of latitudes ±80° in the (e) thick and (f) thin shell models. Solid (dashed) colored lines indicate dynamo (non-magnetic) models. Solid black lines indicate the conductive temperature profile, following Kono and Roberts (2001). (For interpretation of the references to color in this figure legend, the reader is referred to the web version of this article.)

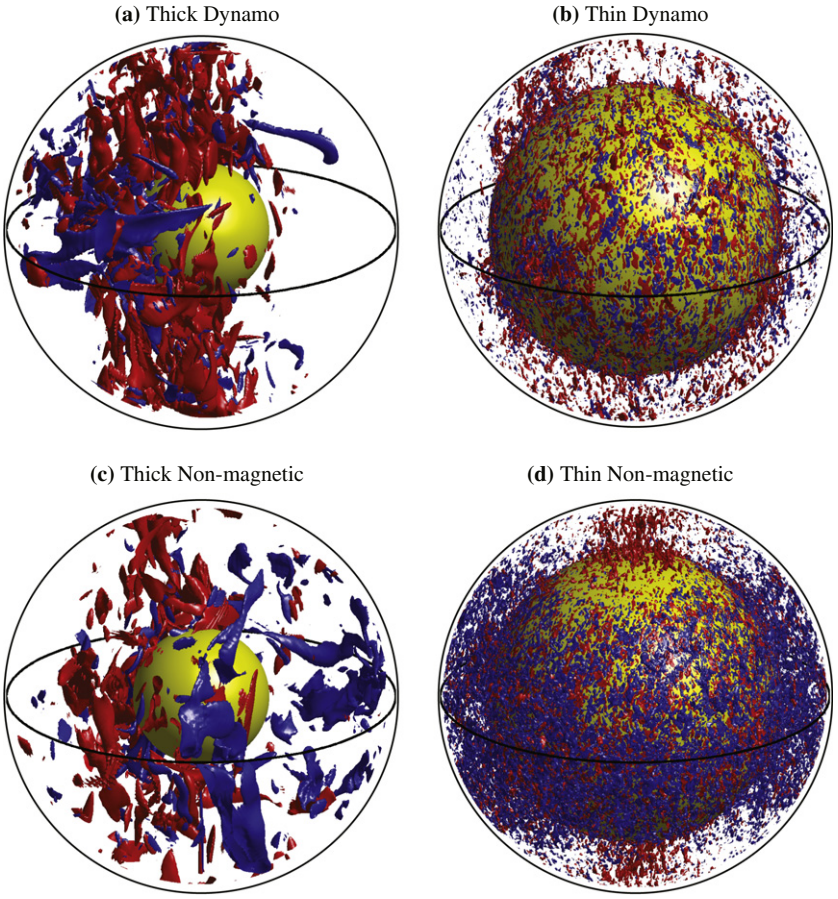

Fig. 6. Axial vorticity isosurfaces at levels $|\omega_z| = 1.6 \times 10^4$ (thick shell) and $|\omega_z| = 2.6 \times 10^4$ (thin shell). Red (blue) indicates cyclonic (anticyclonic) vorticity. The inner yellow sphere represents the inner core, and the boundary layers have been excluded for clarity. (For interpretation of the references to color in this figure legend, the reader is referred to the web version of this article.)

summarizes the results by giving the dimensionless output parameters.

4.1. Characteristics of the magnetic field

Fig. 3 shows the temporal evolution of the dynamo through time series of magnetic energy density and dipole latitude. Both dynamos tend to vary strongly with time; there is an average of one reversal or excursion every $0.04\tau_\eta$ ($0.01\tau_\eta$) in the thick (thin) shell dynamo. In addition, both dynamos are dominated by non-axisymmetric magnetic energy throughout the whole core (>90%), with equipartioning between toroidal and poloidal components in the outer core and more prominent toroidal components in the inner core.

Fig. 4 (top row) shows snapshots of radial magnetic field intensity near the outer shell boundary in our models. These visualizations illustrate that the multipolar magnetic fields are dominated by poorly organized, small-scale, locally intense flux patches. In contrast, the time-averaged, axisymmetric toroidal magnetic fields and poloidal magnetic field lines show that large-scale, persistent features also develop in both dynamo models with amplitudes that are substantially weaker than the instantaneous flux patches (Fig. 4, bottom row). These mean magnetic fields also tend to have flux concentrated in a single hemisphere when averaged over 0.02 (0.004) magnetic diffusion times in the thick (thin) dynamo model. This occurs because the axisymmetric dipole, quadrupole, and octupole components are all significant in our models (Fig. 10; Grote et al., 1999).

The characteristic wavenumber of the magnetic fields, $\overline{k_B}$, is calculated from the magnetic spectra:

$$\overline{k_B} = \sqrt{\overline{l_B}^2 + \overline{m_B}^2}, \tag{12a}$$

$$\text{where } \overline{l_B} = \sum_{l=0}^{l=l_{max}} \frac{l(\mathbf{B}_l \cdot \mathbf{B}_l)}{2\mathscr{E}_M}, \tag{12b}$$

$$\text{and } \overline{m_B} = \sum_{m=0}^{m=m_{max}} \frac{m(\mathbf{B}_m \cdot \mathbf{B}_m)}{2\mathscr{E}_M}. \tag{12c}$$

Here, $\mathbf{B}_l$ is magnetic induction at spherical harmonic degree l, $\mathbf{B}_m$ is magnetic induction at spherical harmonic order m, and $\mathscr{E}_M$ is the magnetic energy density. Table 3 gives these wavenumbers for our models and shows that $\overline{k_B}$ is about a factor of three times greater in the thin shell model. This difference is primarily a consequence of geometrical effects (Heimpel et al., 2005a).

The dynamic Elsasser number characterizes the ratio of Lorentz to Coriolis forces in dynamos and can be used as a measure of magnetic field strength:

$$\Lambda_d = \frac{B^2}{2\rho\mu_o \Omega U \ell_B}, \tag{13}$$

where $\ell_B \sim (\pi D/2)/\overline{k_B}$ is the typical quarter-wavelength of magnetic field variations (Soderlund et al., 2012). The magnetic field strengths differ between the thick and thin shell dynamo models in Fig. 4, where flux patches tend to be roughly an order of magnitude stronger in the thin shell model. While the dynamic Elsasser number near the outer shell boundary is always less than unity in

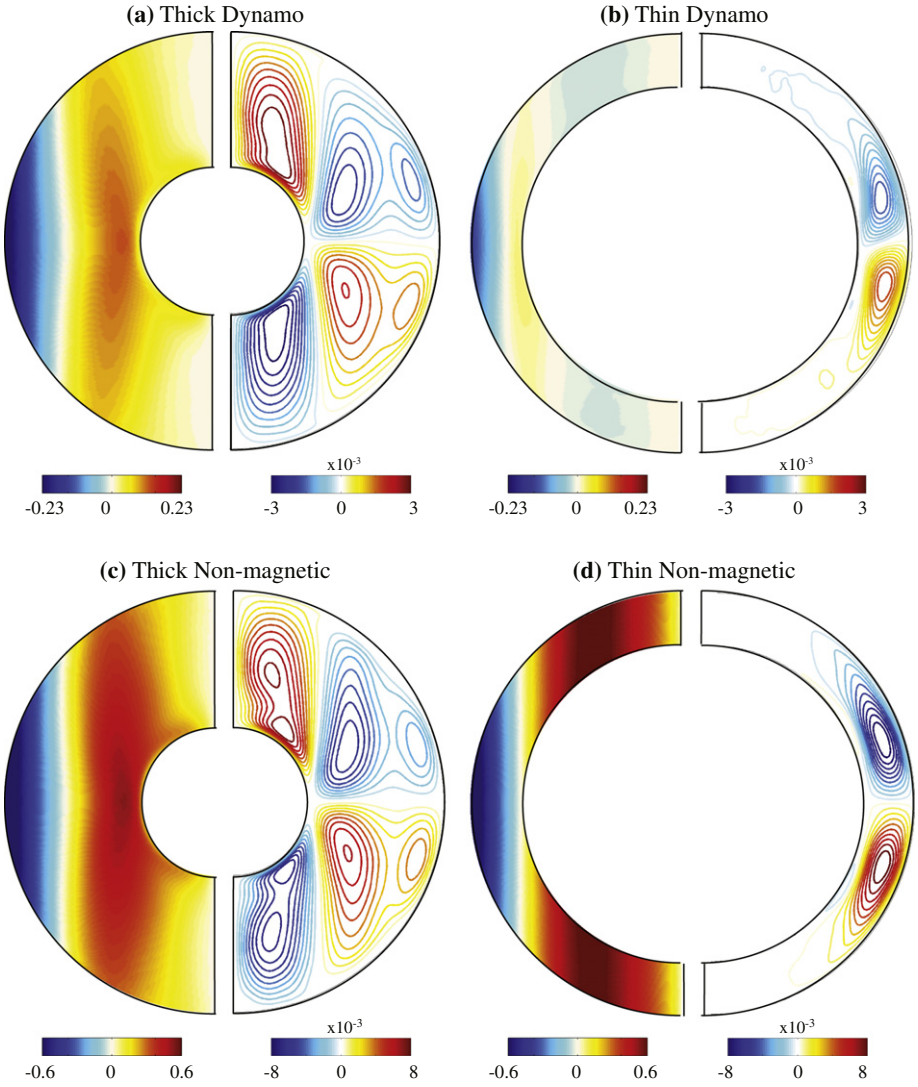

Fig. 7. Time-averaged zonal flows (left panels) and meridional circulations (right panels). Red (blue) indicates both prograde (retrograde) zonal motions and clockwise (counterclockwise) meridional circulations. Flow speeds are given in zonal Rossby number units, $Ro_{ZF} = U_\phi/2\Omega D$. (For interpretation of the references to color in this figure legend, the reader is referred to the web version of this article.)

the thick shell model, Λ_d can locally exceed unity in the thin shell model. When averaged over the entire fluid volume, however, both models have $\Lambda_d < 0.2$ as shown in Table 3, predicting the Lorentz force to have a secondary influence on the convective (non-zonal) dynamics.

4.2. Characteristics of the temperature field

Convective heat transfer efficiency is measured by the Nusselt number. Convection is more efficient in the thin shell models, where $Nu \approx 25$, than in the thick shell models, where $Nu \approx 15$. This occurs because the thin shell models are more strongly supercritical ($Ra = 190Ra_c$) than the thick shell models ($Ra = 110Ra_c$).

Convection also modifies the global temperature field. Fig. 5 shows the time-averaged, axisymmetric temperature in our models (top row) and plots the mean temperature as a function of radius at the equator and the average of ±80° latitude (bottom row). The equatorial regions are thermally well-mixed in all of our models, while substantial radial gradients occur at high latitudes, especially in the non-magnetic cases. In addition, the mean bulk temperature is cooler in the thick shell models. King et al. (2010) also observed this trend in well-mixed systems and attribute the mean bulk temperature reduction with increased shell thickness to the conservation of heat flux across the inner and outer shells.

4.3. Characteristics of the velocity field

Fig. 6 shows snapshots of axial vorticity $\omega_z = \hat{\mathbf{z}} \cdot (\nabla \times \mathbf{u})$ isosurfaces in the bulk fluid of our models. Independent of the presence of magnetic fields and differences in shell geometry, convection is characterized by poorly organized, three-dimensional flows in all of our models, rather than by columnar structures aligned with the rotation axis as is typical for rotationally dominated models.

The characteristic wavenumbers of the flow structures are calculated from the kinetic spectra analogously to (12) and are given in Table 3. Typical wavenumbers are comparable between the dynamo and non-magnetic models, but are about five times smaller-scale in the thin shell compared to the thick shell models. This trend is similar to that observed for magnetic field length scales, where geometrical effects are primarily responsible for the different length scales (Al-Shamali et al., 2004; Heimpel et al., 2005a).

Fig. 7 shows the time-averaged, axisymmetric meridional circulations in our models (right panels). Two large circulation cells

develop outside of the tangent cylinder in all of our simulations. These cells have poleward flow near the outer boundary and equatorward flow near the inner boundary, resulting in an equatorial upwelling and downwellings at mid-latitudes. Cells also develop above and below the inner core with opposite polarities in the thick shell geometry, promoting the mid-latitude downwellings and leading to upwellings near both poles. In contrast, meridional circulations are weak within the tangent cylinder of the thin shell models because isotherms are nearly flat within the tangent cylinder (Fig. 5).

The time-averaged, axisymmetric zonal flows are also compared in Fig. 7 (left panels). This comparison shows that all simulated zonal flows are characterized by retrograde equatorial jets, despite differences in electrical conductivity and shell geometry. Prograde flows also develop at high latitudes in all models except the thin shell dynamo. In this case, magnetic fields strongly modify the zonal flows, leading to a weak prograde jet near the tangent cylinder and retrograde jets near the rotation axis.

5. Analysis of results

In this section we discuss how the magnetic fields, heat transfer patterns, meridional circulations, and zonal flows are generated in our models.

5.1. Magnetic field generation

Magnetic field generation occurs on both local and global scales (e.g., Cattaneo, 1999). Mean-field dynamos result when the fluid motions promote field generation at scales larger than that of the convection. Zonal flows shear poloidal magnetic fields to form toroidal magnetic fields via the Ω-effect, and helical motions create poloidal magnetic fields by twisting toroidal field lines via the α-effect (e.g., Moffatt, 1978; Miesch, 2005). In contrast, fluctuating dynamos result when fluid motions stretch and amplify magnetic fields at scales smaller than that of turbulence (e.g., Subramanian, 1997; Schekochihin et al., 2005; Kleeorin and Rogachevskii, 2011).

Typical length scales of the magnetic and flow fields are quantified using the characteristic wavenumbers, $\overline{k_u}$ and $\overline{k_B}$, given in Table 3. Regardless of shell geometry, we find that the magnetic field is smaller scale than the velocity field ($\overline{k_B} \gtrsim 3\overline{k_u}$). This scale disparity suggests that the magnetic fields in our models are generated by small-scale, fluctuating dynamo action. Furthermore, the time-averaged magnetic energy spectra are strongly dominated by the non-axisymmetric component, containing more than 90% of the energy in both dynamo models. This weak mean field contribution is consistent with a fluctuating dynamo system.

5.2. Thermal emissions and meridional circulation generation

The heat Eq. (7) describes how thermal energy is transported. In a turbulent system, the variables can be decomposed into mean and fluctuating components: $T = \overline{T} + T'$ and $\mathbf{u} = \bar{\mathbf{u}} + \mathbf{u}'$ for temperature and velocity. The mean quantities are temporally averaged and the fluctuating quantities are assumed to have zero mean over time (e.g., Kundu and Cohen, 2002). Averaging (7) then yields the mean heat equation:

$$\frac{\partial \overline{T}}{\partial t} = -\nabla \cdot \left(\bar{\mathbf{u}}\overline{T} + \overline{\mathbf{u}'T'} - \frac{1}{Pr}\nabla \overline{T} \right), \tag{14}$$

recast in terms of heat fluxes. The terms on the right side are, respectively, mean convective heat flux, turbulent convective heat flux, and molecular heat flux. These processes control the thermal emission pattern.

Radial heat transfer is decomposed into mean, turbulent, and total (mean plus turbulent) convective components in Fig. 8. The equatorial peak in convective heat transfer is robust across all cases, while the behavior at high latitudes exhibits larger variations with shell thickness. In the thick shell models, radially outward heat transfer is enhanced near the equator and poles by the meridional circulations and, to a lesser extent, by turbulent motions. The thin shell models behave differently due to the lack of polar circulation cells. In these cases, the Hadley-like cells dictate the mean pattern, leading to a prominent peak in heat transfer near the equator. Interestingly, the turbulent patterns differ between the thin dynamo and non-magnetic cases. While both profiles have low latitude peaks, the minima occur at mid-latitudes in the dynamo model and at the poles in the non-magnetic model. This result implies that the magnetic fields modify the correlation between the fluctuating radial velocity and temperature fields.

Equatorial Hadley-like cells affect the temperature at high latitudes in our thick shell models. This leads to a substantial latitudinal temperature gradient near the poles (Fig. 5a and b), which drives an azimuthal thermal wind flow and associated polar upwelling (e.g., Olson et al., 1999; Aurnou et al., 2003; Aubert, 2005; Miesch, 2005). In contrast, Hadley-like cells in the thin shell models (Fig. 5c and d) do not strongly affect the polar regions such

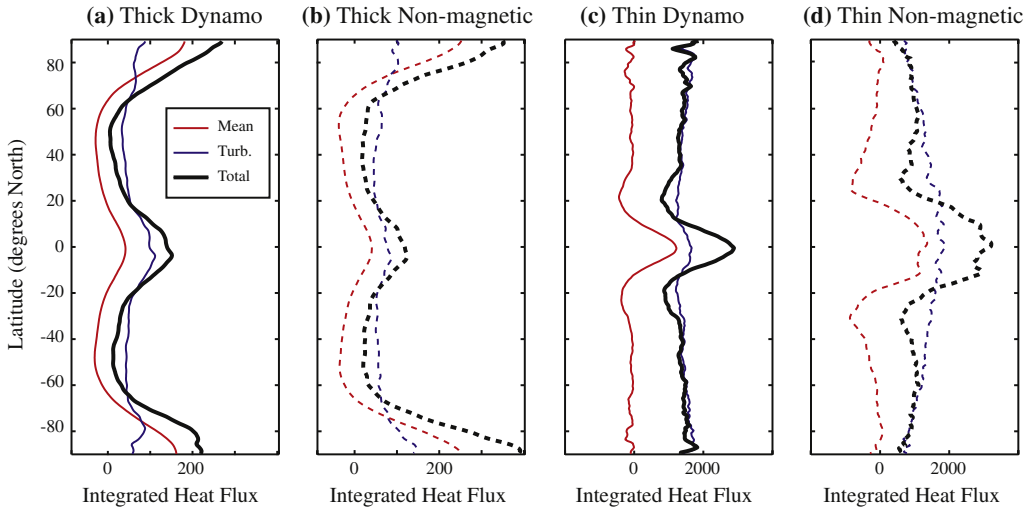

Fig. 8. Non-dimensional mean ($\overline{u_r}\overline{T}$), turbulent ($\overline{u_r'T'}$), and total ($\overline{u_r}\overline{T} + \overline{u_r'T'}$) convective heat transfer integrated over all longitudes and radial levels.

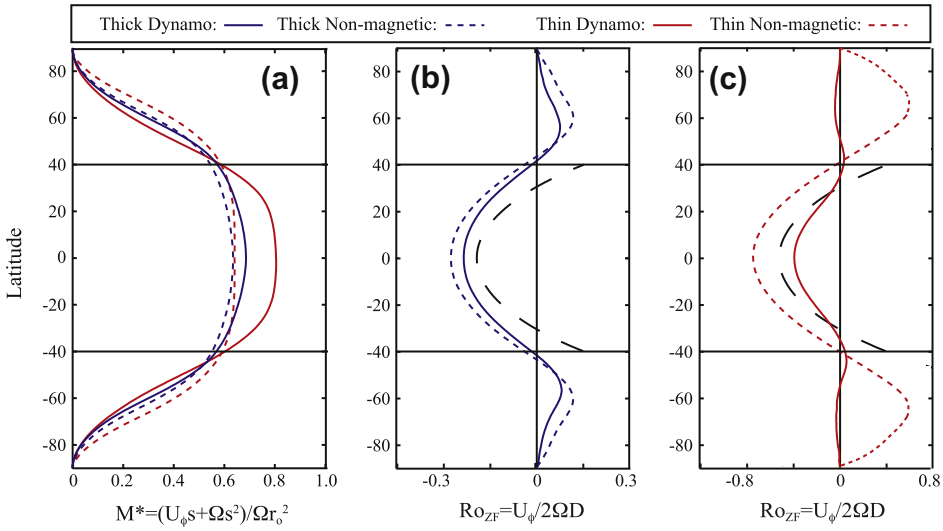

Fig. 9. (a) Dimensionless absolute angular momentum on the outer shell boundaries. Mixing of absolute angular momentum is limited to within about ±40° (solid horizontal lines). Comparison of time-averaged zonal flow profiles to those predicted by angular momentum homogenization when mixing occurs in regions exterior to 40° latitude in the (b) thick and (c) thin shell models. The predicted profiles are indicated by dashed black lines and calculated from Eqs. (11) and (13) of Aurnou et al. (2007).

that neither a thermal wind nor a polar upwelling is generated, explaining why no polar cells develop in this geometry.

5.3. Zonal flow generation

Turbulent flows can mix absolute angular momentum, leading to the development of retrograde equatorial jets (e.g., Gilman and Foukal, 1979; Suomi et al., 1991; Aurnou et al., 2007; Miesch and Hindman, 2011; Gastine et al., 2012). This hypothesis also makes predictions of the equatorial jet speed depending on the shell geometry and what fraction of the fluid volume has homogenized absolute angular momentum. Fig. 9a plots the dimensionless absolute angular momentum, M^*, on the outer shell boundary as a function of latitude. Angular momentum mixing occurs in all of our simulations, where M^* is constant within about ±40° latitude in all models except the thin shell dynamo, which is approximately constant within ±20° latitude. Panels b and c of Fig. 9 compare our simulated zonal wind profiles in the thick and thin shell models, respectively, against those predicted by angular momentum mixing exterior to ±40° latitude. Good agreement between the simulated and predicted profiles occurs at low latitudes, supporting this zonal flow generation hypothesis. At high latitudes, however, the profiles diverge because the predicted flows approach infinity near the poles. Instead, the winds are damped with no flow at the poles. Strong magnetic damping is also evident in the thin shell dynamo model (Fig. 9c).

Zonal flow power budgets have shown that zonal power is primarily dissipated by viscosity in the absence of magnetic fields, while both viscous and magnetic dissipation can be important in dynamos (Aubert, 2005; Stanley and Mohammadi, 2008). As a result, magnetic fields may be expected to strongly damp the zonal flows when the ratio of zonal Lorentz to zonal viscous forces exceeds unity. Following Soderlund et al. (2012), we explicitly calculate these forces to determine their ratio a posteriori. Towards this end, the axisymmetric azimuthal forces are integrated over the meridional (r,θ) hemisphere:

$$F^{\phi} = \int_0^{\pi} \int_{r_i}^{r_o} |\mathscr{F}(r,\theta)| r^2 \sin\theta \, dr \, d\theta, \tag{15}$$

where $\mathscr{F}(r,\theta)$ is a generic force density given by each term in the zonal momentum equation.

This zonal Lorentz to viscous force ratio, $Q_{\phi} = F_L^{\phi}/F_V^{\phi}$, is calculated to be 0.8 in the thick shell dynamo model and 2.9 in the thin shell dynamo. Consequently, the zonal flows are similar between the dynamo and non-magnetic ice giant-style models in the thick shell geometry because viscous damping exceeds magnetic damping, while the zonal flows differ more strongly in the thin shell geometry because magnetic damping exceeds viscous damping. In both cases, more than 99% of F_L^{ϕ} is due to fluctuating magnetic fields, such that magnetic damping by the mean field is negligible.

6. Comparison of model results against observations

Surface magnetic spectra of Uranus and Neptune are compared against time-averaged and instantaneous simulated spectra in Fig. 10. Both planets and models have significant power in the dipole, quadrupole, and octupole components. The planets have a strong $m = 1$ signature and much weaker power at higher orders. The randomly chosen instantaneous spectra are non-axisymmetric, yet both models have peak power in the axisymmetric $m = 0$ mode when temporally averaged. This result suggests that the magnetic fields of Uranus and Neptune may have a prominent axisymmetric component when averaged over time.

It is important to note, however, that our models artificially assume that the dynamo source regions extend through the molecular envelopes to the planetary surfaces. Consequently, attenuation of the magnetic field is not taken into account. This attenuation, which increases with spherical harmonic degree, occurs in the weakly conducting deep atmosphere and approximates that for a potential field. Additional attenuation and filtering of high degree and rapidly varying field components would occur in stably stratified layers of relatively high electrical conductivity outside the dynamo region (Christensen, 2006; Christensen and Wicht, 2008; Stanley and Mohammadi, 2008). As a result, the magnetic field at the planet surface will be larger scale and weaker than at the top of the dynamo region.

Fig. 11 illustrates the thick shell model results. The dynamo model self-consistently generates magnetic field, thermal emission, and zonal flow patterns that are qualitatively similar to those of the ice giants (Fig. 2): a multipolar dynamo, peak thermal emission in the equatorial and polar regions, and a retrograde zonal jet

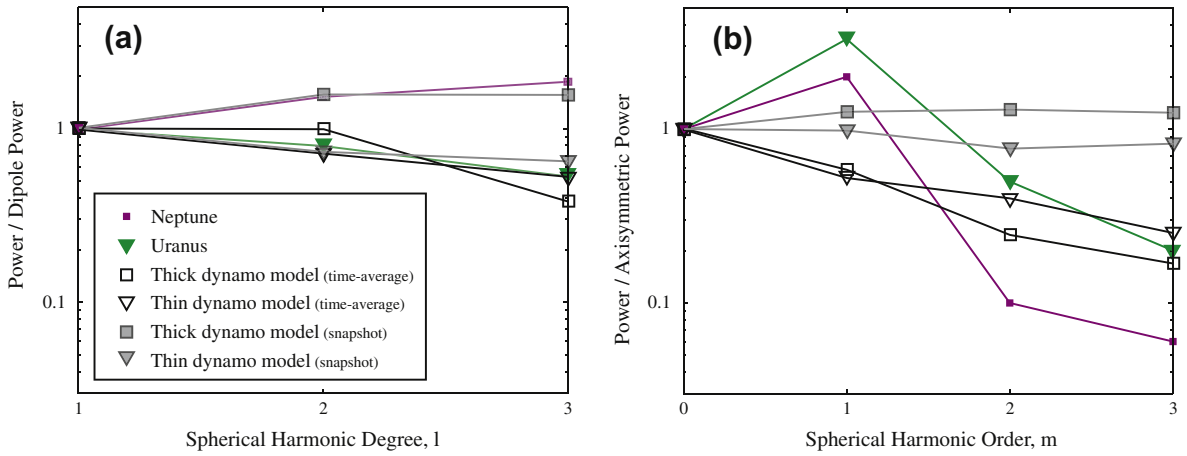

Fig. 10. Comparison of (instantaneous) observed versus randomly selected (gray filled symbols) and time-averaged (black hollow symbols) simulated magnetic power spectra taken at the outer shell boundary up to spherical harmonic degree and order three. (a) Spectra normalized by the dipolar ($l = 1$) power. (b) Spectra normalized by the axisymmetric ($m = 0$) power.

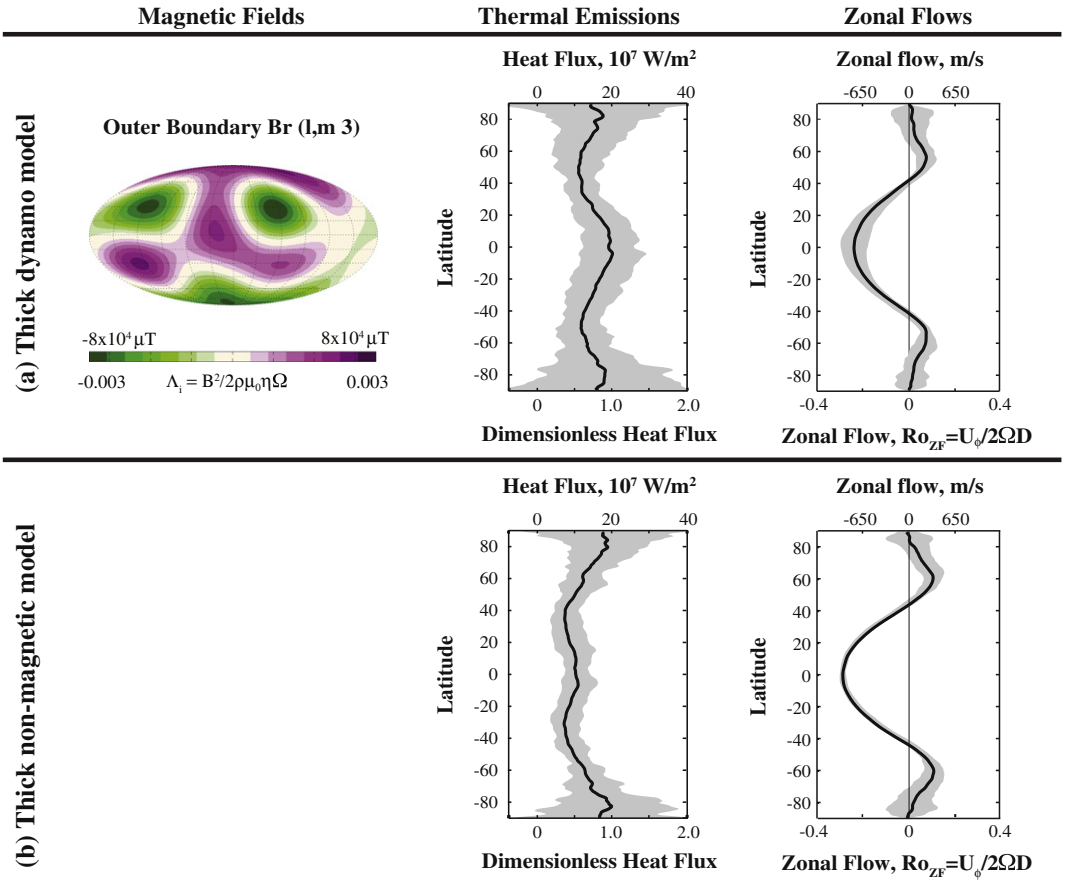

Fig. 11. Simulated radial magnetic fields ($l, m \leqslant 3$), heat fluxes, and zonal flows for the thick shell (a) dynamo and (b) non-magnetic models. Magnetic fields are instantaneous. The heat fluxes and zonal flows in bold are the time averages of at least 20 snapshots, while the shaded regions indicate two standard deviations. The dimensionless thermal emission profiles have been normalized by the maximum mean values.

at low latitudes with flanking prograde jets at high latitudes. The magnetic field exhibits significant temporal variations, but remains multipolar irrespective of the temporal averaging window (Fig. 10). Shaded regions in the width of two standard deviations indicate time variability of the thermal emission and zonal flow profiles and show that thermal emissions also evolve strongly with time, while the zonal flows are quasi-steady.

Fig. 12 illustrates the thin shell model results to test the robustness of the dynamics to differences in convective-region geometry. While the magnetic field, thermal emission, and zonal flow patterns tend to be qualitatively similar in the thick and thin shell models, there are two noteworthy differences. First, the heat flux pattern in the non-magnetic model captures only the equatorial peak with a minima occurring at the poles. The second and

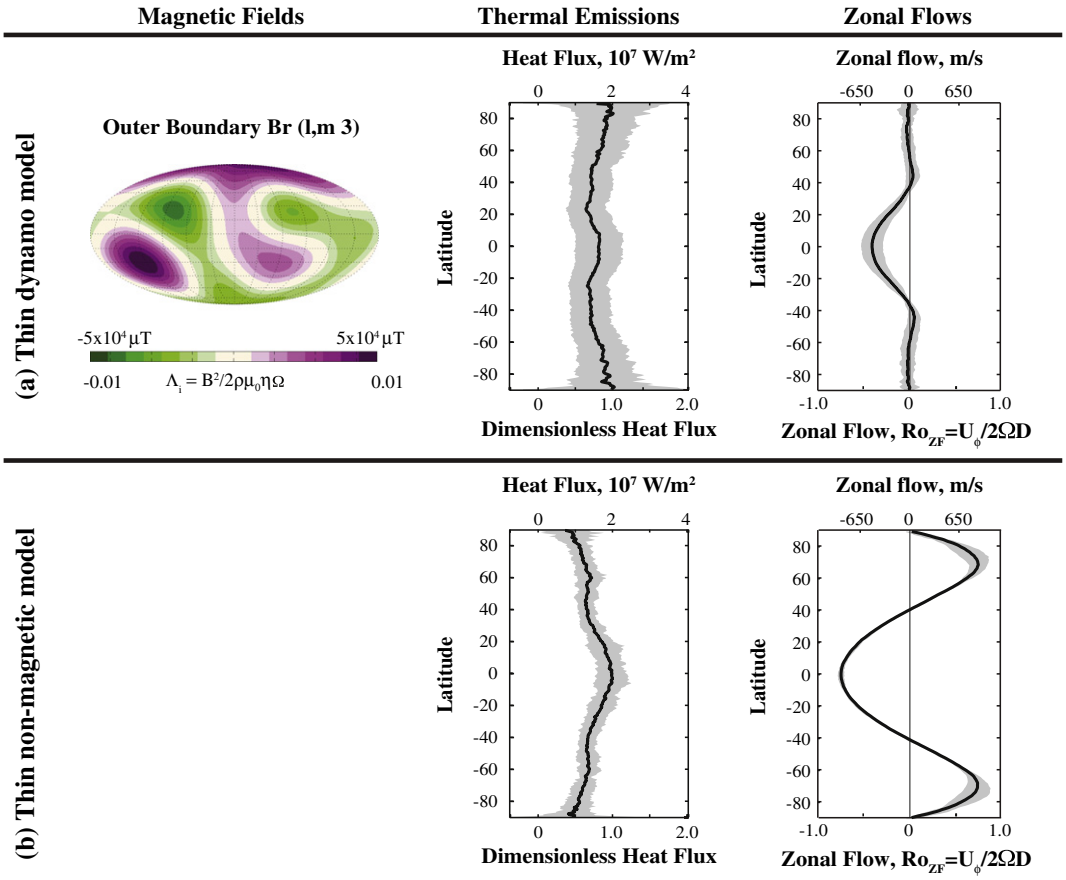

Fig. 12. Simulated radial magnetic fields ($l, m \leqslant 3$), heat fluxes, and zonal flows for the thin shell (a) dynamo and (b) non-magnetic models. Magnetic fields are instantaneous. The heat fluxes and zonal flows in bold are the time averages of at least 20 snapshots, while the shaded regions indicate two standard deviations. The dimensionless thermal emission profiles have been normalized by the maximum mean values.

dominant deviation compared to the observations is the lack of strong prograde zonal jets at high latitudes in the dynamo model, contradicting the unified layer hypothesis. We anticipate, however, that if a thin electrically insulating layer were present near the outer boundary in our model, prograde jets would be generated near the surface at high latitudes since such jets develop in the non-magnetic model, bringing the zonal flow pattern into qualitative agreement with the observations. Furthermore, magnetic damping of zonal flows is artificially strong in our models with $Pm = 1$ compared to low Pm solutions that are more appropriate to the ice giants (Gomez-Perez and Heimpel, 2007; Soderlund, 2011). Consequently, it may not be appropriate to use these results to constrain the shell thickness of the combined molecular envelope and dynamo region. Instead, this suggests that further studies in this regime should be carried out using models with radially varying fluid properties and lower Pm to test the viability of thin shell models for explaining ice giants observations.

We also contrast the simulated amplitudes against the observations, similar to the dimensional analysis of Section 3.3. The mean radial field strengths at the outer boundaries are on the order of $\Lambda_i \sim 10^{-3}$ in both dynamo models when truncated at spherical harmonic degree $l = 3$ to match the resolution limit of the observations. If we instead assume $r_o = 0.8R_P$ such that the outer boundaries correspond to the tops of the dynamo regions, upward continuation to the planet surfaces yields $\Lambda_i \sim 10^{-4}$. In contrast, the mean observed intensities are $\Lambda_i \sim 5 \times 10^{-5}$ at the ice giant surfaces and $\Lambda_i \sim 10^{-4}$ at the tops of the dynamo regions. Note that these planetary values assume ice giant magnetic diffusivity estimates, not the much larger model values. The simulated strengths of the large-scale magnetic fields are then comparable to the observed intensities of Uranus and Neptune.

The simulated heat flux is many orders of magnitude larger than the observed heat flux. However, no overdriving may be necessary when the results are scaled to more realistic material properties (e.g., to lower Ekman numbers) as discussed in Section 3.3.

Peak dimensionless model speeds are $|Ro_{ZF}| \sim 0.3$ in the thick shell models, $|Ro_{ZF}| \sim 0.4$ in the thin dynamo model, and $|Ro_{ZF}| \sim 0.7$ in the thin non-magnetic model. These speeds are similar to those of the ice giants, which have $|Ro_{ZF}| \sim 0.25 \pm 0.15$ given the possible range in wind speeds due to uncertainties in the planets' rotation rates.

We utilize the Boussinesq approximation, and the consequences of this limitation must be assessed. Our zonal flows and meridional circulations are qualitatively similar to those obtained in the non-magnetic, anelastic models of Brun and Palacios (2009) and Gastine et al. (2012) simulating non-magnetic, slowly rotating convection with a density difference between the upper and lower boundaries of up to two orders of magnitude (about five density scale heights). Since we have estimated that the dynamo and molecular envelopes of Uranus and Neptune contain about six density scale heights, the similarity between our Boussinesq and these anelastic models suggests that density stratification will not fundamentally alter the dynamics. Furthermore, Gastine and Wicht (2012) and Gastine et al. (2012) show that the buoyancy force strongly increases with radius for non-magnetic rotating convection models with high density stratifications. This increase suggests that poorly organized convection becomes easier to achieve in the ice giants outside of the dynamo region. In contrast, we

argue that it is of primary importance to consider electrical conductivity stratification in giant planet dynamo models (e.g., Gomez-Perez et al., 2010; Heimpel and Gomez-Perez, 2011) since the Lorentz force can significantly modify the zonal flows and heat transfer.

7. Discussion and conclusions

Uranus and Neptune are unique in the Solar System. Observations show that these planets have magnetic fields, internal heat fluxes, and zonal winds that are fundamentally different from those of Jupiter and Saturn. We argue that these differences may arise from a lack of rotational organization of the convective flows from which they arise. Towards testing this hypothesis, we carry out turbulent dynamo and non-magnetic rotating convection models with two spherical shell geometries. In these simulations, magnetic fields are generated by fluctuating dynamos due to the small-scale, poorly organized nature of the convection. The simulated zonal flows are characterized by retrograde equatorial jets. These, we argue, result from the homogenization of absolute angular momentum mixing via convective turbulence. Meridional circulations are coupled to radial heat transport and lead to peak heat flux near the equator and additionally near the poles in the thick shell geometry. Thus, we predict local equatorial peaks in internal heat fluxes on Uranus and Neptune. Our dynamo models then self-consistently generate magnetic field, thermal emission, and zonal flow patterns that are roughly comparable to those of Uranus and Neptune. No other models, to our knowledge, are able to self-consistently and simultaneously produce these large-scale dynamical characteristics of the ice giants.

It has also been argued that dynamo action in the ice giants occurs in relatively thin layers that lie above convectively stable ionic oceans (Stanley and Bloxham, 2004, 2006). In this hypothesis, multipolar magnetic fields are generated because a stable layer of fluid can dynamically respond to electromagnetic stresses. In contrast, a large, solid, electrically conducting inner core can effectively anchor the dipole field (e.g., Hollerbach and Jones, 1993). This argument then implies that a stably stratified fluid core is required for multipolar dynamo generation in both Uranus and Neptune. Recent internal structure models, however, do not necessarily support the presence of such a region in Neptune (Fortney et al., 2011; Nettelmann et al., 2012). Our results also appear to contradict this hypothesis since multipolar dynamos are produced despite the presence of large, solid, electrically conducting inner cores. Interestingly, the Stanley and Bloxham (2004, 2006) models meet the $Ro_c \gtrsim 1$, $\Psi_{King} \gtrsim 1$, $\Psi_{Julien} \gtrsim 1$ criteria, but neither of the Ψ_{ST} criteria. Our results may then differ because their models employ strong hyperdiffusion and do not simulate the non-axisymmetric inertia terms in the momentum equation (Kuang and Bloxham, 1999).

Two directions for future work are evident. First, it is important to deconvolve what controls the transitions in magnetic field morphology, heat transfer, zonal flow, and local-scale convection and how these transitions scale to planetary settings (e.g., Sprague et al., 2006; King et al., 2009, 2010, 2012; Schmitz and Tilgner, 2009, 2010; Tilgner, 2012; Julien et al., 2012a,b; Soderlund et al., 2012; Gastine et al., 2012). Second, the next step to make the models presented here more planet-like is to incorporate radially varying electrical conductivity and, secondarily, density (e.g., Stanley and Glatzmaier, 2010; Gomez-Perez et al., 2010; Heimpel and Gomez-Perez, 2011). This will allow both the electrically insulating molecular envelope and the electrically conducting ionic ocean to be simulated in a single model.

The most advanced studies of rotating convection suggest that three-dimensional turbulence may develop in planetary-scale water-rich layers, such as the dynamo regions of Uranus and Neptune. Based upon this argument, we have carried out dynamo models here with three-dimensional convective turbulence and find that strongly multipolar dynamo generation is easily excited in these systems. Extrapolating our results to bodies other than Uranus and Neptune, we predict that strongly multipolar magnetic fields will be observed on extrasolar ice giant planets and slowly rotating red giant branch stars (e.g., Gillon et al., 2008; Leitzinger et al., 2011; Brun and Palacios, 2009).

Acknowledgments

We thank Julien Aubert and an anonymous referee for their thoughtful reviews, as well as Keith Julien, Gerald Schubert, and Johannes Wicht for helpful suggestions. This research was funded by the NASA Planetary Atmospheres Program (Grants NNX09AB61G and NNX09AB57G) and the National Science Foundation (Grants EAR-0944312 and AAG-0909206). K.M.S. acknowledges the support of the University of Texas Institute for Geophysics (UTIG) Postdoctoral Fellowship Program, and E.M.K. acknowledges the support of the Miller Institute for Basic Research in Science. Computational resources supporting this work were provided by the NASA High-End Computing (HEC) Program through the NASA Advanced Supercomputing (NAS) Division at Ames Research Center. This is UTIG contribution 2559.

References

Al-Shamali, F., Heimpel, M.H., Aurnou, J.M., 2004. Varying the spherical shell geometry in rotating thermal convection. Geophys. Astrophys. Fluid Dyn. 98, 153–169.
Anderson, B.J. et al., 2011. The global magnetic field of Mercury from messenger orbital observations. Science 30, 1859–1862.
Anderson, B.J. et al., 2012. Low-degree structure in Mercury's planetary magnetic field. J. Geophys. Res. 117, E00L12. http://dx.doi.org/10.1029/2012JE004159.
Aubert, J., 2005. Steady zonal flows in spherical shell dynamos. J. Fluid Mech. 542 (October), 53–67.
Aurnou, J.M., Andreadis, S., Zhu, L., Olson, P.L., 2003. Experiments on convection in Earth's core tangent cylinder. Earth Planet. Sci. Lett. 212, 119–134.
Aurnou, J.M., Heimpel, M.H., Wicht, J., 2007. The effects of vigorous mixing in a convective model of zonal flow on the ice giants. Icarus 190, 110–126.
Aurnou, J.M., Heimpel, M.H., Allen, L., King, E.M., Wicht, J., 2008. Convective heat transfer and the pattern of thermal emission on the gas giants. Geophys. J. Int. 173, 793–801.
Bessolaz, N., Brun, A.S., 2011. Hunting for giant cells in deep stellar convective zones using wavelet analysis. Astrophys. J. 728, 15. http://dx.doi.org/10.1088/0004-637X/728/2/115.
Brun, A.S., Palacios, A., 2009. Numerical simulations of a rotating red giant star. I. Three-dimensional models of turbulent convection and associated mean flows. Astrophys. J. 702, 1078–1097.
Buffett, B.A., Christensen, U.R., 2007. Magnetic and viscous coupling at the core–mantle boundary: Inferences from observations of the Earth's nutations. Geophys. J. Int. 171, 145–152.
Burton, M.E., Dougherty, M.K., Russell, C.T., 2009. Model of Saturn's internal planetary magnetic field based on Cassini observations. Planet. Space Sci. 57, 1706–1713.
Calkins, M.A., Aurnou, J.M., Eldredge, J.D., Julien, K., 2012. The influence of fluid properties on the morphology of core turbulence and the geomagnetic field. Earth Planet. Sci. Lett. 359–360, 55–60.
Cattaneo, F., 1999. On the origin of magnetic fields in the quiet photosphere. Astrophys. J. 515, L39–L42.
Cavazzoni, C., Chiarotti, G.L., Scandolo, S., Tosatti, E., Bernasconi, M., Parrinello, M., 1999. Superionic and metallic states of water and ammonia at giant planet conditions. Science 283, 44–46.
Chau, R., Hamel, S., Nellis, W.J., 2011. Chemical processes in the deep interior of Uranus. Nature Commun. 2 (203). http://dx.doi.org/10.1038/ncomms1198.
Christensen, U.R., 2006. A deep dynamo generating Mercury's magnetic field. Nature 444, 1056–1058.
Christensen, U.R., Aubert, J., 2006. Scaling properties of convection driven dynamos in rotating spherical shells and application to planetary magnetic fields. Geophys. J. Int. 166, 97–114.
Christensen, U.R., Wicht, J., 2007. Numerical dynamo simulations. In: Olson, P.L. (Ed.), Treatise on Geophysics, vol. 8. Elsevier, pp. 245–282.
Christensen, U.R., Wicht, J., 2008. Models of magnetic field generation in partly stable planetary cores: Applications to Mercury and Saturn. Icarus 196, 16–34.
Christensen, U.R., Olson, P.L., Glatzmaier, G.A., 1999. Numerical modeling of the geodynamo: A systematic parameter study. Geophys. J. Int. 138, 393–409.
Desch, M.D., Connerney, J.E.P., Kaiser, M.L., 1986. The rotation period of Uranus. Nature 322, 42–43.

Dharmaraj, G., Stanley, S., 2012. Effect of inner core conductivity on planetary dynamo models. Phys. Earth Planet. Int. http://dx.doi.org/10.1016/j.pepi.2012.09.003.
Fortney, J.J., Ikoma, M., Nettelmann, N., Guillot, T., Marley, M.S., 2011. Self-consistent model atmospheres and the cooling of the Solar System's giant planets. Astrophys. J. 729, 32–46.
Fry, P.M., Sromovsky, L.A., de Pater, I., Hammel, H.B., Rages, K.A., 2012. Detection and tracking of subtle cloud features on Uranus. Astrophys. J. 143, 150–162.
Gastine, T., Wicht, J., 2012. Effects of compressibility on driving zonal flow in gas giants. Icarus. arXiv:1203.4145v1.
Gastine, T., Wicht, J., Aurnou, J.M., 2012. Zonal flow regimes in rotating anelastic spherical shells: An application to giant planets. arXiv:1211.3246 [astro-ph.EP].
Gilman, P.A., 1977. Nonlinear dynamics of Boussinesq convection in a deep rotating spherical shell – I. Geophys. Astrophys. Fluid Dyn. 8, 93–135.
Gilman, P.A., 1978. Nonlinear dynamics of Boussinesq convection in a deep rotating spherical shell – II. Geophys. Astrophys. Fluid Dyn. 11, 157–179.
Gilman, P.A., Foukal, P.V., 1979. Angular velocity gradients in the solar convection zone. Astrophys. J. 229, 1179–1185.
Gillon, M. et al., 2008. Detection of transits of the nearby hot Neptune GJ 436 b. Astron. Astrophys. 472, L13–L16.
Gomez-Perez, N., Heimpel, M.H., 2007. Numerical models of zonal flow dynamos: An application to the ice giants. Geophys. Astrophys. Fluid Dyn. 101, 371–388.
Gomez-Perez, N., Heimpel, M.H., Wicht, J., 2010. Effects of a radially varying electrical conductivity on 3d numerical dynamos. Phys. Earth Planet. Int. 181, 42–53.
Grote, E., Busse, F.H., Tilgner, A., 1999. Convection-driven quadrupolar dynamos in rotating spherical shells. Phys. Rev. E 60, 5025–5028.
Grote, E., Busse, F.H., Tilgner, A., 2000. Regular and chaotic spherical shell dynamos. Phys. Earth Planet. Int. 117, 259–272.
Guervilly, C., Cardin, P., Schaeffer, N., 2011. A dynamo driven by zonal jets at the upper surface: Applications to giant planets. Icarus. arXiv:1106.2701v1.
Guillot, T., 1999. Interiors of giant planets inside and outside the Solar System. Science 286, 72–77.
Gurnett, D.A. et al., 2007. The variable rotation period of the inner region of Saturn's plasma disk. Science 316, 442–445.
Gurnett, D.A. et al., 2009. Discovery of a north–south asymmetry in Saturn's radio rotation period. Geophys. Res. Lett. 361, L16102.
Hammel, H.B., Rages, K., Lockwood, G.W., Karkoschka, E., de Pater, I., 2001. New measurements of the winds of Uranus. Icarus 153, 229–235.
Hammel, H.B., de Pater, I., Gibbard, S., Lockwood, G.W., Rages, K., 2005. Uranus in 2003: Zonal winds, banded structure, and discrete features. Icarus 175, 534–545.
Heimpel, M.H., Gomez-Perez, N., 2011. On the relationship between zonal jets and dynamo action in giant planets. Geophys. Res. Lett. 38, L14201.
Heimpel, M.H., Aurnou, J.M., Al-Shamali, F., Gomez-Perez, N., 2005a. A numerical study of dynamo action as a function of spherical shell geometry. Earth Planet. Sci. Lett. 236, 542–557.
Heimpel, M.H., Aurnou, J.M., Wicht, J., 2005b. Simulation of equatorial and high-latitude jets on Jupiter in a deep convection model. Nature 483, 193–196.
Helled, R., Anderson, J.D., Schubert, G., 2010. Uranus and Neptune: Shape and rotation. Icarus 210, 446–454.
Helled, R., Anderson, J.D., Podolak, M., Schubert, G., 2011. Interior models of Uranus and Neptune. Astrophys. J. 726, 15–22.
Hollerbach, R., Jones, C.A., 1993. Influence of the Earth's inner core on geomagnetic fluctuations and reversals. Nature 365, 541–543.
Holme, R., Bloxham, J., 1996. The magnetic fields of Uranus and Neptune: Methods and models. J. Geophys. Res. 101, 2177–2200.
Holme, R., Ingersoll, A.P., 1994. Baroclinic instability in the interiors of the giant planets: A cooling history of Uranus? Icarus 110, 340–356.
Hubbard, W.B., Nellis, W.J., Mitchell, A.C., Holmes, N.C., Limaye, S.S., McCandless, P.C., 1991. Interior structure of Neptune: Comparison with Uranus. Science 253, 648–651.
Jones, C.A., 2011. Planetary magnetic fields and fluid dynamos. Annu. Rev. Fluid Mech. 43, 583–614.
Jones, C.A., Kuzanyan, K.M., 2009. Compressible convection in the deep atmospheres of giant planets. Icarus 358, 873–897.
Jones, C.A., Boronski, P., Brun, A.S., Glatzmaier, G.A., Gastine, T., Miesch, M.S., Wicht, J., 2011. Anelastic convection-driven dynamo benchmarks. Icarus 216, 120–135.
Julien, K., Knobloch, E., Rubio, A.M., Vasil, G.M., 2012a. Heat transport in low-Rossby-number Rayleigh–Bénard convection. Phys. Rev. Lett. 109, 5. http://dx.doi.org/10.1103/PhysRevLett.109.254503.
Julien, K., Rubio, A.M., Grooms, I., Knobloch, E., 2012b. Statistical and physical balances in low Rossby number Rayleigh–Bénard convection. Geophys. Astrophys. Fluid Dyn. 106, 392–428.
Käpylä, P.J., Mantere, M.J., Guerrero, G., Brandenburg, A., Chatterjee, P., 2011. Reynolds stress and heat flux in spherical shell convection. Astron. Astrophys. 531, 17. http://dx.doi.org/10.1051/0004-6361/201015884.
Karkoschka, E., 2011. Neptune's rotational period suggested by the extraordinary stability of two features. Icarus 215, 439–448.
Kaspi, Y., Hubbard, W.B., Showman, A.P., Flierl, G.R., 2009. Gravitational signature of Jupiter's internal dynamics. Geophys. Res. Lett. 37, L01204.
King, E.M., Aurnou, J.M., 2012. Thermal evidence for Taylor columns in turbulent, rotating Rayleigh–Bénard convection. Phys. Rev. E 85, 11. http://dx.doi.org/10.1103/PhysRevE.85.016313.
King, E.M., Stellmach, S., Noir, J., Hansen, U., Aurnou, J.M., 2009. Boundary layer control of rotating convection systems. Nature 457, 301–304.
King, E.M., Soderlund, K.M., Christensen, U.R., Wicht, J., Aurnou, J.M., 2010. Convective heat transfer in planetary dynamo models. Geochem. Geophys. Geosyst. 11, 19. http://dx.doi.org/10.1029/2010GC003053.
King, E.M., Stellmach, S., Aurnou, J.M., 2012. Heat transfer by rapidly rotating Rayleigh–Bénard convection. J. Fluid Mech. 691, 568–582.
Kivelson, M.G. et al., 1996. Discovery of Ganymede's magnetic field by the Galileo spacecraft. Nature 384, 537–541.
Kleeorin, N., Rogachevskii, I., 2011. Growth rate of small-scale dynamo at low magnetic Prandtl numbers. ArXiv e-prints.
Knudson, M.D. et al., 2012. Probing the interiors of the ice giants: Shock compression of water to 700 GPa and 3.8 g/cm^3. Phys. Rev. Lett. arXiv:1201.2622v1.
Kono, M., Roberts, P.H., 2001. Definition of the Rayleigh number for geodynamo simulation. Phys. Earth Planet. Int. 128, 13–24.
Kuang, W., Bloxham, J., 1999. Numerical modelling of magnetohydrodynamic convection in a rapidly rotating spherical shell: Weak and strong field dynamo action. J. Comput. Phys. 153, 51–81.
Kundu, P.K., Cohen, I.M., 2002. Fluid Mechanics. Elsevier Science.
Kutzner, C., Christensen, U.R., 2000. Effects of driving mechanisms in geodynamo models. Geophys. Res. Lett. 27, 29–32.
Kutzner, C., Christensen, U.R., 2002. From stable dipolar towards reversing numerical dynamos. Phys. Earth Planet. Int. 131, 29–45.
Lee, K.K.M. et al., 2006. Laser-driven shock experiments on precompressed water: Implications for icy giant planets. J. Chem. Phys. 125, 7. http://dx.doi.org/10.1063/1.2207618.
Leitzinger, M. et al., 2011. Could CoRoT-7b and Kepler-10b be remnants of evaporated gas or ice giants? Planet. Space Sci. 59, 1472–1481.
Levine, J.S., Kraemer, D.R., Kuhn, W.R., 1977. Solar radiation incident on Mars and the outer planets: Latitudinal, seasonal, and atmospheric effects. Icarus 31, 136–145.
Lian, Y., Showman, A.P., 2010. Generation of equatorial jets by large-scale latent heating on the giant planets. Icarus 207, 373–393.
Martin, S.C., de Pater, I., Marcus, P., 2012. Neptune's zonal winds from near-IR Keck adaptive optics imaging in August 2001. Astrophys. Space Sci. 337, 65–78.
Miesch, M.S., 2005. Large-scale dynamics of the convection zone and tachocline. Living Rev. Sol. Phys. <http://www.livingreviews.org/lrsp-2005-1>.
Miesch, M.S., Hindman, B.W., 2011. Gyroscopic pumping in the solar near-surface shear layer. Astrophys. J. 743, 79–104.
Moffatt, H.K., 1978. Magnetic Field Generation in Electrically Conducting Fluids. Cambridge University Press, Cambridge.
Ness, N.F. et al., 1986. Magnetic fields at Uranus. Science 233, 85–89.
Ness, N.F., Acuña, M.H., Burlaga, L.F., Connerney, J.E.P., Lepping, R.P., Neubauer, F.M., 1989. Magnetic fields at Neptune. Science 246, 1473–1478.
Ness, N.F., Runcorn, S.K., Miller, S., 1994. Intrinsic magnetic fields of the planets: Mercury to Neptune. Philos. Trans. R. Soc. Lond. Ser. A 349, 249–260.
Nettelmann, N., Helled, R., Fortney, J.J., Redmer, R., 2012. New indication for a dichotomy in the interior structure of Uranus and Neptune from the application of modified shape and rotation data. Planet. Space Sci., in press. http://dx.doi.org/10.1016/j.pss.2012.06.019
Olson, P.L., Christensen, U.R., 2006. Dipole moment scaling for convection-driven planetary dynamos. Earth Planet. Sci. Lett. 250, 561–571. http://dx.doi.org/10.1038/ncomms1198.
Olson, P.L., Christensen, U.R., Glatzmaier, G.A., 1999. Numerical modeling of the geodynamo: Mechanisms of field generation and equilibration. J. Geophys. Res. 104, 10383–10404.
Pearl, J.C., Conrath, B.J., 1991. The albedo, effective temperature, and energy balance of Neptune, as determined from Voyager data. J. Geophys. Res., Suppl. 96, 18921–18930.
Pearl, J.C., Conrath, B.J., Hanel, R.A., Pirraglia, J.A., 1990. The albedo, effective temperature, and energy balance of Uranus as determined from Voyager IRIS data. Icarus 84, 12–28.
Pirraglia, J.A., 1984. Meridional energy balance of Jupiter. Icarus 59, 169–176.
Podolak, M., Hubbard, W.B., Stevenson, D.J., 1991. Models of Uranus' interior and magnetic field. In: Bergstralh, J.T., Miner, E.D., Matthews, M.S. (Eds.), Uranus. University of Arizona Press, Tucson.
Porco, C.C. et al., 2003. Cassini imaging of Jupiter's atmosphere, satellites and rings. Science 299, 1541–1547.
Redmer, R., Mattsson, T.R., Nettelmann, N., French, M., 2011. The phase diagram of water and the magnetic fields of Uranus and Neptune. Icarus 211, 798–803.
Roberts, P.H., Aurnou, J.M., 2012. On the theory of core–mantle coupling. Geophys. Astrophys. Fluid Dyn. 106, 157–230.
Russell, C.T., Dougherty, M.K., 2010. Magnetic fields of the outer planets. Space Sci. Rev. 152, 251–269.
Ruzmaikin, A.A., Starchenko, S.V., 1991. On the origin of Uranus and Neptune magnetic fields. Icarus 93, 82–87.
Schekochihin, A.A., Haugen, N.E.L., Brandenburg, A., Cowley, S.C., Maron, J.L., McWilliams, J.C., 2005. The onset of a small-scale turbulent dynamo at low magnetic Prandtl numbers. Astrophys. J. 625, L115–L118.
Schmitz, S., Tilgner, A., 2009. Heat transport in rotating convection without ekman layers. Phys. Rev. E 80, 4. http://dx.doi.org/10.1103/PhysRevE.80.015305.
Schmitz, S., Tilgner, A., 2010. Transitions in turbulent rotating Rayleigh–Bènard convection. Geophys. Astrophys. Fluid Dyn. 104, 481–489.
Schubert, G., Soderlund, K.M., 2011. Planetary magnetic fields: Observations and models. Phys. Earth Planet. Int. 187, 92–108.

Simitev, R.D., Busse, F.H., 2005. Prandtl-number dependence of convection-driven dynamos in rotating spherical fluid shells. J. Fluid Mech. 532, 365–388.
Smith, B.A. et al., 1986. Voyager 2 in the uranian system: Imaging science results. Science 233, 43–64.
Smith, B.A. et al., 1989. Voyager 2 at Neptune: Imaging science results. Science 246, 1422–1449.
Soderlund, K.M., 2011. Investigating Transitions in Planetary Dynamo Models. Ph.D. Thesis, University of California, Los Angeles.
Soderlund, K.M., King, E.M., Aurnou, J.M., 2012. The influence of magnetic fields in planetary dynamo models. Earth Planet. Sci. Lett., 9–20.
Sprague, M., Julien, K., Knobloch, E., Werne, J., 2006. Numerical simulation of an asymptotically reduced system for rotationally constrained convection. J. Fluid Mech. 551, 141–174.
Sreenivasan, B., Jones, C.A., 2006. The role of inertia in the evolution of spherical dynamos. Geophys. J. Int. 164, 467–476.
Sromovsky, L.A., Fry, P.M., Dowling, T.E., Baines, K.H., Limaye, S.S., 2001. Neptune's atmospheric circulation and cloud morphology: Changes revealed by 1998 HST imaging. Icarus 150, 244–260.
Sromovsky, L.A., Fry, P.M., Hammel, H.B., Ahue, W.M., de Pater, I., Rages, K.A., Showalter, M.R., van Dam, M.A., 2009. Uranus at equinox: Cloud morphology and dynamics. Icarus 203, 265–286.
Stanley, S., Bloxham, J., 2004. Convective-region geometry as the cause of Uranus' and Neptune's magnetic fields. Nature 428, 151–153.
Stanley, S., Bloxham, J., 2006. Numerical dynamo models of Uranus' and Neptune's unusual magnetic fields. Icarus 184, 556–572.
Stanley, S., Glatzmaier, G.A., 2010. Dynamo models for planets other than Earth. Space Sci. Rev. 153, 617–649.
Stanley, S., Mohammadi, A., 2008. Effects of an outer thin stably stratified layer on planetary dynamos. Phys. Earth Planet. Int. 168, 179–190.
Stevenson, D.J., 1978. The outer planets and their satellites. In: Dermott, S.F. (Ed.), The Origin of the Solar System. Wiley, New York, pp. 395–431.
Stevenson, D.J., 1983. Planetary magnetic fields. Rep. Prog. Phys. 46, 555–620.
Subramanian, K., 1997. Dynamics of fluctuating magnetic fields in turbulent dynamos incorporating ambipolar drifts. Astrophysics. ArXiv e-prints.
Sukoriansky, S., Galperin, B., Dikovskaya, N., 2002. Universal spectrum of two-dimensional turbulence on a rotating sphere and some basic features of atmospheric circulation on giant planets. Phys. Rev. Lett. 89, 4. http://dx.doi.org/10.1103/PhysRevLett.89.124501.
Suomi, V.E., Limaye, S.S., Johnson, D.R., 1991. High winds of Neptune: A possible mechanism. Science 251, 929–932.
Takehiro, S.-I., Yamada, M., Hayashi, Y.-Y., 2011. Retrograde equatorial surface flows generated by thermal convection confined under a stably stratified layer in a rapidly rotating spherical shell. Geophys. Astrophys. Fluid Dyn. 105, 61–81.
Tilgner, A., 2012. Transitions in rapidly rotating convection driven dynamos. Phys. Rev. Lett. 109, 4. http://dx.doi.org/10.1103/PhysRevLett.109.248501.
Warwick, J.W. et al., 1989. Voyager planetary radio astronomy at Neptune. Science 246, 1498–1501.
Weiss, S., Stevens, R.J.A.M., Zhong, J.-Q., Clercx, H.J.H., Lohse, D., Ahlers, G., 2010. Finite-size effects lead to supercritical bifurcations in turbulent rotating Rayleigh–Bénard convection. Phys. Rev. Lett. 105, 4. http://dx.doi.org/10.1103/PhysRevLett.105.224501.
Wicht, J., 2002. Inner-core conductivity in numerical dynamo simulations. Phys. Earth Planet. Int. 132, 281–302.
Yu, Z.J., Leinweber, H., Russell, C.T., 2010. Galileo constraints on the secular variation of the jovian magnetic field. J. Geophys. Res. 115, E03002.
Zhang, K., Schubert, G., 2000. Magnetohydrodynamics in rapidly rotating spherical systems. Annu. Rev. Fluid Mech. 32, 409–443.
Zhang, K., Schubert, G., 2002. From penetrative convection to teleconvection. Astrophys. J. 572, 461–476.
Zhong, J.-Q., Ahlers, G., 2010. Heat transport and the large-scale circulation in rotating turbulent Rayleigh–Bénard convection. J. Fluid Mech. 665, 300–333.